Neuron

Article

Divergent brainstem opioidergic pathways that coordinate breathing with pain and emotions

Highlights

- PBL^{Oprm1} neurons regulate breathing, affective pain, and anxiety in mice
- PBL^{Oprm1} neurons constitute projection-defined core and shell subpopulations
- Core and shell PBL^{Oprm1} neurons differentially regulate breathing, pain, and anxiety
- Core and shell PBL^{Oprm1} neurons form a local recurrent excitatory network

Authors

Shijia Liu, Mao Ye, Gerald M. Pao, ...,
Sukjae J. Kang, Dong-Il Kim, Sung Han

Correspondence

sunghan@salk.edu

In brief

Breathing can be influenced by pain and anxiety, but the neural substrate underlying this connection is unknown. Liu et al. report that neurons in the lateral parabrachial nucleus expressing the μ-opioid receptor coordinate breathing with affective pain and negative emotions through divergent output circuits and local recurrent networks in mice.

Liu et al., 2022, Neuron *110*, 857–873
March 2, 2022
https://doi.org/10.1016/j.neuron.2021.11.029

Neuron

CellPress

Article

Divergent brainstem opioidergic pathways that coordinate breathing with pain and emotions

Shijia Liu,[1,2] Mao Ye,[1] Gerald M. Pao,[3] Samuel M. Song,[2] Jinho Jhang,[1] Haibei Jiang,[2] Jong-Hyun Kim,[1] Sukjae J. Kang,[1] Dong-Il Kim,[1] and Sung Han[1,2,4,*]
[1]Peptide Biology Laboratory, The Salk Institute for Biological Studies, La Jolla, CA 92037, USA
[2]Section of Neurobiology, Division of Biological Sciences, University of California, San Diego, La Jolla, CA 92093, USA
[3]Molecular and Cellular Biology Laboratory, The Salk Institute for Biological Studies, La Jolla, CA 92037, USA
[4]Lead contact
*Correspondence: sunghan@salk.edu
https://doi.org/10.1016/j.neuron.2021.11.029

SUMMARY

Breathing can be heavily influenced by pain or internal emotional states, but the neural circuitry underlying this tight coordination is unknown. Here we report that *Oprm1* (μ-opioid receptor)-expressing neurons in the lateral parabrachial nucleus (PBL) are crucial for coordinating breathing with affective pain in mice. Individual PBL^{Oprm1} neuronal activity synchronizes with breathing rhythm and responds to noxious stimuli. Manipulating PBL^{Oprm1} activity directly changes breathing rate, affective pain perception, and anxiety. Furthermore, PBL^{Oprm1} neurons constitute two distinct subpopulations in a “core-shell” configuration that divergently projects to the forebrain and hindbrain. Through non-overlapping projections to the central amygdala and pre-Bötzinger complex, these two subpopulations differentially regulate breathing, affective pain, and negative emotions. Moreover, these subsets form recurrent excitatory networks through reciprocal glutamatergic projections. Together, our data define the divergent parabrachial opioidergic circuits as a common neural substrate that coordinates breathing with various sensations and behaviors such as pain and emotional processing.

INTRODUCTION

Breathing is a fundamental, life-sustaining function (Dick et al., 2018). This rhythmic behavior originates from the network activity of the ventrolateral medulla (Ashhad and Feldman, 2020) and contributes to a variety of homeostatic processes, particularly the maintenance of pH and blood O_2/CO_2 levels (Del Negro et al., 2018). To date, most breathing research has focused on the mechanism by which pacemaking networks in medullary respiratory centers generate breathing rhythm (Dick et al., 2018). However, little is known about neural mechanisms regulating changes in breathing rhythm caused by such factors as emotional and sensory stimuli (Boiten et al., 1994). For example, in humans, intense and uncontrollable pain induces hyperventilation (Jafari et al., 2017). Breathing also becomes faster and more shallow with fear (Feleky, 1916) and in psychiatric conditions such as posttraumatic stress disorder, panic attacks, and phobias (Bass and Gardner, 1985). Breathing rhythm can also be controlled by volitional processes, such as sniffing (Moore et al., 2013), vocalizing (Smotherman et al., 2010), swallowing (Bautista et al., 2014), and sighing (Li et al., 2016).

The breathing center most likely to mediate the breathing changes caused by emotional and sensory inputs is the pontine respiratory group (PRG) (Del Negro et al., 2018). Unlike the medullary respiratory groups (Cui et al., 2016; Del Negro et al., 2018; Tan et al., 2010), the PRG is not involved in the direct generation of respiratory rhythms but instead modulates the rate and pattern of breathing (Del Negro et al., 2018; Wang et al., 1957) in response to various forebrain and hindbrain inputs (Dutschmann and Dick, 2012). One crucial component of the PRG is the parabrachial nucleus (PB), a small but heterogeneous nucleus composed of various cytoarchitecturally distinct subnuclei (Fulwiler and Saper, 1984). Direct electrical stimulation of this area, or glutamate injection, altered breathing rhythm in cats (Cohen, 1971) and rats (Chamberlin and Saper, 1994), respectively. Interestingly, alternately facilitatory and inhibitory effects have been reported on this behavior depending on stimulation protocol and location (Chamberlin and Saper, 1994; Cohen, 1971; Dutschmann and Dick, 2012; Navarrete-Opazo et al., 2020). For example, activating the dorsal PB induced tachypnea, whereas the ventral PB—especially the Kölliker-Fuse nucleus—induced variable responses such as apneusis, bradypnea, and tachypnea (Chamberlin, 2004; Chamberlin and Saper, 1994; Dutschmann and Dick, 2012; Dutschmann and Herbert, 2006).

Among the subdivisions of the PB, the lateral PB (PBL, or referred to as PB_L, lPB, PBNl, or lPBN in other papers) is known to relay affective pain signals from the spinal cord to the forebrain (Gauriau and Bernard, 2002; Han et al., 2015). The PBL neurons are mostly glutamatergic (Yokota et al., 2015) and express several specific molecular markers such as *Oprm1*, which encodes the μ-opioid receptor (MOR) (Chamberlin et al., 1999). The MOR is the primary inhibitory opioid receptor mediating opioid-induced analgesia, as *Oprm1*-knockout mice lacked antinociceptive responses to morphine administration (Matthes et al., 1996). The MOR is also highly expressed among the respiratory centers of the brain and is regarded as a primary contributor to opioid-induced respiratory depression (OIRD) (Dahan et al., 2001; Montandon et al., 2011; Prkic et al., 2012). Indeed, conditional deletion of the *Oprm1* gene in the parabrachial complex ameliorates OIRD (Bachmutsky et al., 2020; Liu et al., 2021; Varga et al., 2020). Together, these findings suggest possible roles of the parabrachial MOR-signaling pathway in both pain perception and breathing regulation.

Based on the above observations, we hypothesized that *Oprm1*-expressing neurons in the PBL ($\text{PBL}^{\mathit{Oprm1}}$) coordinate breathing with pain and emotions, as in pain-induced hyperventilation. Using cell-type- and projection-specific circuit dissection approaches that allow us to map, monitor, and manipulate defined neural circuits, we found that $\text{PBL}^{\mathit{Oprm1}}$ neurons regulate breathing rate, affective pain, and anxiety-like behaviors. Furthermore, our results demonstrate that these behaviors are collectively controlled by the recurrent excitatory neural network of two distinct subpopulations of *Oprm1* neurons in the core and shell of the PBL, which diverge to the central amygdala (CeA, the emotion center) and the pre-Bötzinger complex (preBötC, the ventral respiratory center).

RESULTS

$\text{PBL}^{\mathit{Oprm1}}$ activity is highly correlated with breathing

We investigated the role of $\text{PBL}^{\mathit{Oprm1}}$ neurons in breathing by performing concurrent measurements of $\text{PBL}^{\mathit{Oprm1}}$ activity and breathing rhythm in freely moving mice. We monitored breathing via a micro-thermistor sensor implanted in the nasal cavity, which measured temperature fluctuations between inhaled and exhaled air (Biskamp et al., 2017; Nguyen Chi et al., 2016; McAfee et al., 2016; Moberly et al., 2018; Moore et al., 2013) without altering normal breathing rhythm (Figures S1A and S1B). To monitor $\text{PBL}^{\mathit{Oprm1}}$ activity, we delivered a recombinant adeno-associated virus (AAV) encoding the calcium indicator jGCaMP7s in the PBL of $\mathit{Oprm1}^{\mathit{Cre/+}}$ mice and recorded calcium activity with fiber photometry (Figures 1A and 1B; validation for MOR co-expression in Figures S1C and S1D). Strong cross-correlations were observed between $\text{PBL}^{\mathit{Oprm1}}$ activity and breathing rate and plethysmograph amplitude at both second (Figure 1C) and minute scales (Figures 1D, 1E, and 1G). $\text{PBL}^{\mathit{Oprm1}}$ activity closely matched the onset of increases in the plethysmograph amplitude (Figure 1F) and rate (Figure 1H) during bouts of high respiratory activity. Interestingly, sighing (identified by the stereotyped respiratory waveforms) (Li et al., 2016) and sniffing events (identified by the rearing-sniffing behaviors) were also strongly associated with $\text{PBL}^{\mathit{Oprm1}}$ activity (Figures 1D, S1G, and S1H), indicating that $\text{PBL}^{\mathit{Oprm1}}$ neurons are crucial for controlling multiple types of breathing behavior.

To further determine whether this tight correlation is PBL specific and movement independent, we expressed Cre-independent GCaMP6f in the dorsal striatum—a region well known for motor control (Kravitz and Kreitzer, 2012)—and simultaneously recorded calcium and breathing signals in freely moving mice. Dorsal striatum activity was tightly correlated with animals' velocity rather than breathing rate, while $\text{PBL}^{\mathit{Oprm1}}$ activity was tightly coupled with breathing rate even when mice were stationary (Figures S1I and S1J). Finally, to evaluate whether non-$\text{PBL}^{\mathit{Oprm1}}$ populations are also involved in breathing regulation, we injected Cre-off GCaMP6m virus into the PBL of $\mathit{Oprm1}^{\text{Cre/+}}$ mice. The activity of *Oprm1*-negative neurons responded robustly to noxious stimuli (e.g., pinching, Figure S1N) but displayed less correlation with breathing rate and plethysmograph amplitude (Figures S1K–S1M; see also Figures 1E and 1G).

To determine whether this relationship could be leveraged to predict future changes in $\text{PBL}^{\mathit{Oprm1}}$ activity using breathing rhythm (and vice versa), we performed convergent cross-mapping (CCM) analysis (Sugihara et al., 2012). CCM is a manifold-based algorithm that generates predictive models to infer causal relationships of nonlinear time series. When calcium signals were utilized as inputs to generate a CCM model that predicted breathing rate, the predicted trace closely matched the observed trace (Figure 1I), as in the reverse prediction (Figure 1J). However, across different training sets, the model that used calcium to predict breathing performed better than the opposite model (Figure 1K), indicating that $\text{PBL}^{\mathit{Oprm1}}$ neuronal activity provided a stronger driving force to regulate breathing rate than vice versa. These results suggest that the $\text{PBL}^{\mathit{Oprm1}}$ neurons are a causal driver for breathing rate, but breathing, albeit more weakly, also feeds back on $\text{PBL}^{\mathit{Oprm1}}$ neuronal activity.

$\text{PBL}^{\mathit{Oprm1}}$ manipulation alters breathing rate

To further investigate the causal roles of $\text{PBL}^{\mathit{Oprm1}}$ neurons in breathing regulation, we manipulated their activity using both chemogenetic and optogenetic approaches in awake and anesthetized mice (Figures 2A and 2G). Chemogenetic activation of $\text{PBL}^{\mathit{Oprm1}}$ neurons via hM3Dq using clozapine N-oxide (CNO) produced significant increases in breathing rate (Figures 2B, 2C, 2D, and S2B) but did not change plethysmograph amplitude (Figure S2C). Conversely, inhibiting $\text{PBL}^{\mathit{Oprm1}}$ neurons with hM4Di produced significant decreases in breathing rate (Figures 2E, 2F, and S2H) and increases in plethysmograph amplitude (Figure S2I), possibly via compensatory effects mediated by medullary synergistic microcircuits (Cui et al., 2016). CNO effects were confirmed by *ex vivo* slice electrophysiological recordings with cell-attached or whole-cell configurations (Figures S2A and S2G).

To eliminate confounding factors that indirectly affect breathing in awake animals, such as affective state or movement, we also tested the role of $\text{PBL}^{\mathit{Oprm1}}$ neurons in breathing regulation using optogenetics in isoflurane-anesthetized animals while simultaneously monitoring breathing via a piezoelectric sensor (Levitt et al., 2015) (Figures 2G and 2H). Photostimulating $\text{PBL}^{\mathit{Oprm1}}$ neurons with ChR2 significantly increased both breathing rate and plethysmograph amplitude in a frequency-dependent manner (Figures 2I, 2J, 2M, 2N, and S2D–S2F). Conversely, photoinhibition with ArchT suppressed breathing rate in a light-intensity-dependent manner (Figures 2K, 2L, 2O, 2P, and S2J) without affecting the plethysmograph amplitude (Figures S2K and S2L). However, repeated photoinhibition

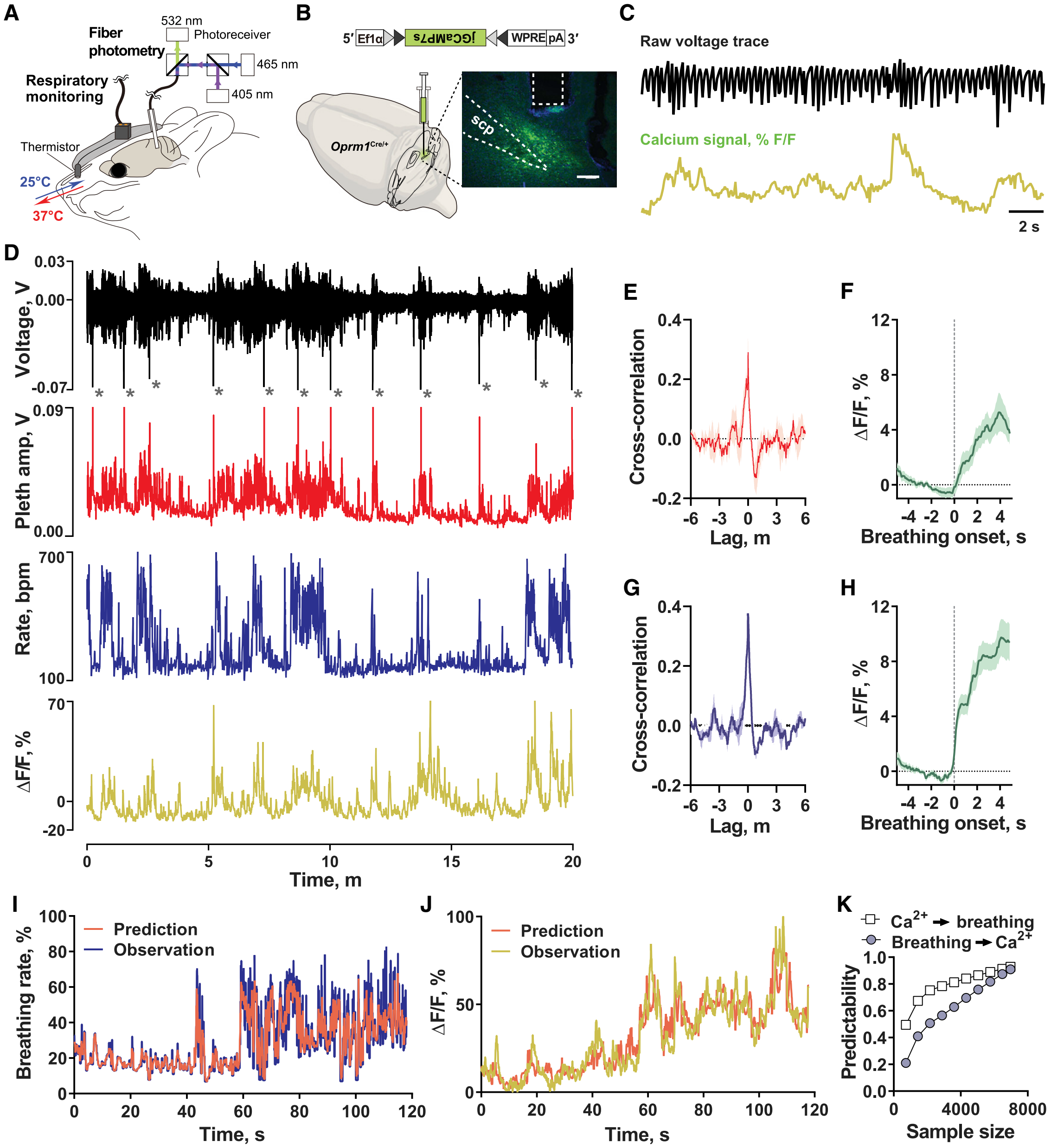

Figure 1. PBL^{Oprm1} activity synchronizes with breathing

(A) Schematic of the simultaneous recording of breathing and neural activity.

(B) Schematic and histology of jGCaMP7s expression in PBL^{Oprm1} neurons. Scale, 200 μm.

(C) 20 s example traces of breathing sensor voltage (top) and PBL^{Oprm1} activity (bottom) illustrating their tight correlation. Scale, 2 s.

(D) 20 min example traces of the raw voltage trace, plethysmograph amplitude, breathing rate, and PBL^{Oprm1} calcium signals (top to bottom), showing their tight correlation. Asterisks indicate sighing events.

(E and G) Strong correlation between calcium signals and plethysmograph amplitude (E) and breathing rate (G) (n = 4).

(F and H) PBL^{Oprm1} activities synchronized with plethysmograph amplitude (F) and breathing rate (H) during major respiratory bouts.

(I and J) PBL^{Oprm1} activities predicted breathing rate (I) and vice versa (J) as shown by CCM analysis.

(K) CCM model using calcium signal to predict breathing rate performed better than the reverse model across different training sample sizes. Data are presented as mean ± SEM. See also Figure S1.

resulted in apnea in some test mice (Figure S2M), suggesting that more potent PBL^{Oprm1} inhibition could simultaneously reduce breathing rate and plethysmograph amplitude. Together, these data suggest that PBL^{Oprm1} neurons are necessary and sufficient for the regulation of breathing—specifically breathing rate—across a wide range of physiological states.

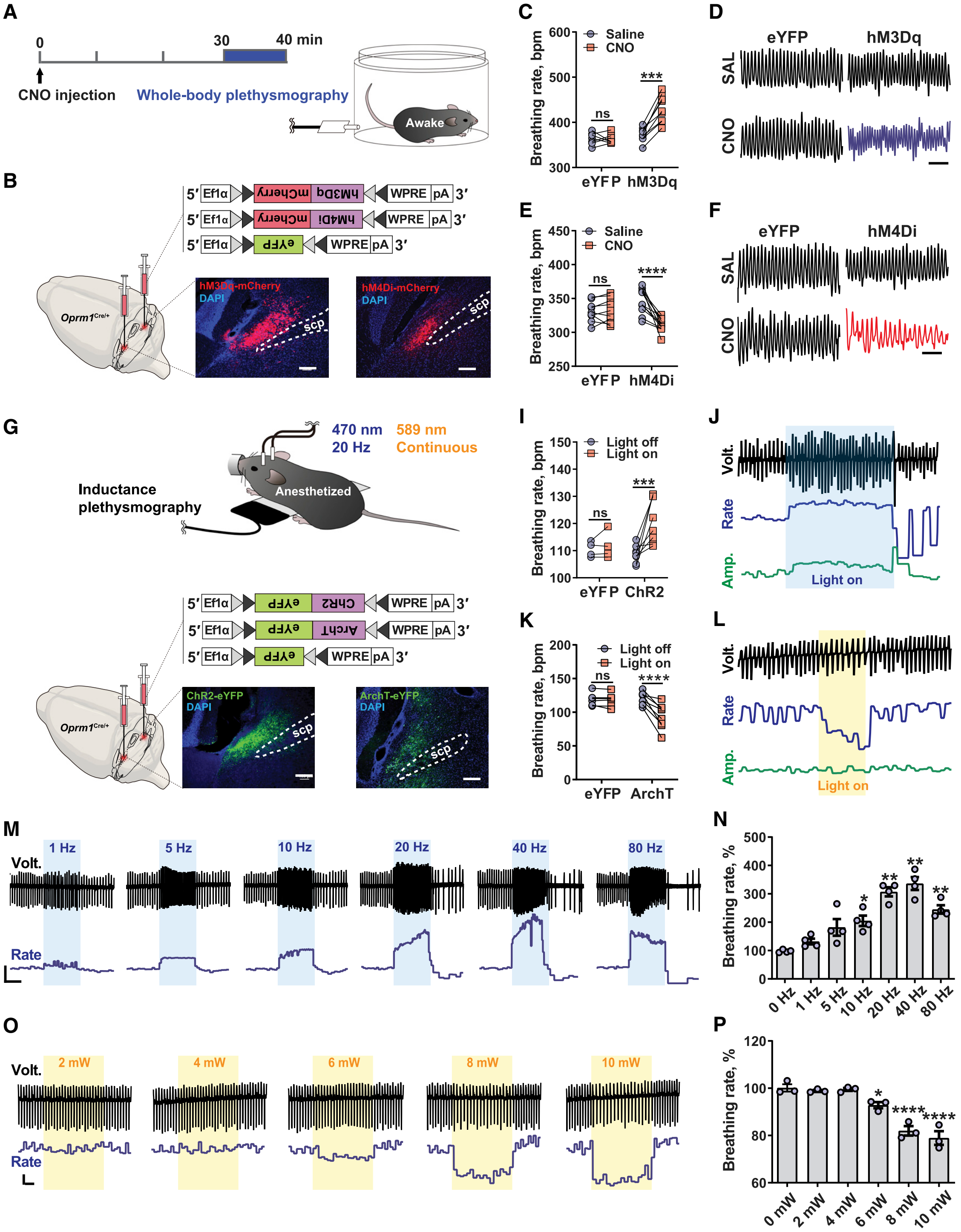

Figure 2. PBL^{Oprm1} neurons regulate breathing rate

(A) Schematic of the use of whole-body plethysmography (WBP) to monitor breathing in awake mice with chemogenetic manipulation.

(B) Schematic and histology of hM3Dq and hM4Di expression in PBL^{Oprm1} neurons. Scale, 200 μm.

(C and E) CNO injection (5 mg/kg intraperitoneally [i.p.]) significantly increased breathing rate in hM3Dq-expressing mice (n = 9, C) and decreased breathing rate in hM4Di-expressing mice (n = 12, E) but did not affect controls expressing enhanced yellow fluorescence protein (eYFP) (n = 7 for C and n = 9 for E).

(D and F) Representative breathing traces after systemic injection of saline or CNO in hM3Dq (D) or hM4Di (F)-expressing mice and eYFP controls. Scale, 1 s.

(G) Schematic of the use of inductance plethysmography to monitor breathing in anesthetized mice with optogenetic manipulation.

(H) Schematic and histology of ChR2 and ArchT expression in PBL^{Oprm1} neurons. Scale, 200 μm.

(legend continued on next page)

Input-output anatomical mapping of PBL^{Oprm1} neurons

Next, we sought to identify direct presynaptic inputs of PBL^{Oprm1} neurons, which could reveal the conditions under which breathing may be modulated. We performed monosynaptic retrograde tracing with G-deleted pseudotyped rabies virus (RVdG), which labels all upstream neurons with red fluorescence (Figure 3A) (Callaway and Luo, 2015). The specificity of our viral tools was demonstrated by the high MOR co-expression in starter cells (96.7% ± 1.2%, n = 3 mice, total 186 cells) (Figure S3A) and a negligible number of mCherry-positive cells in wild-type controls (4 ± 2.65 cells, n = 3 mice) (Figure S3B). Our rabies-tracing results revealed a wide range of PBL^{Oprm1} upstream regions throughout the brain (Figures 3A and 3B), including limbic areas—e.g., the central nucleus of the amygdala (CeA), the bed nucleus of the stria terminalis (BNST), and the parvocellular subparafascicular nucleus (SPFp)—as well as areas relaying sensory and autonomic inputs—e.g., the superior colliculus (SC), the nucleus tractus solitarius (NTS), and the spinal cord (Figures 3A and S3C) (Gauriau and Bernard, 2002; Janak and Tye, 2015; Pautrat et al., 2018; Sahibzada et al., 1986). These data suggest that PBL^{Oprm1} neurons may modulate breathing in response to diverse sensory and emotional challenges.

We also investigated the projection patterns of PBL^{Oprm1} neurons by visualizing their ChR2:eYFP-expressing axon terminals (Figure S3D). Interestingly, many of the PBL^{Oprm1} output regions send reciprocal projections to PBL^{Oprm1} neurons, echoing previous reports of the tightly interconnected central autonomic network of PBL, CeA, BNST, and hypothalamus (Saper and Loewy, 1980) and the PBL-preBötC breathing network (Dutschmann and Dick, 2012; Herbert et al., 1990).

Among these outputs, we further characterized the PBL^{Oprm1} projections to the preBötC, the central rhythm and pattern generator of breathing (Ashhad and Feldman, 2020; Smith et al., 1991). We expressed AAVs Cre-dependently expressing tdTomato in the nucleus and synaptophysin-eGFP fusion protein in the axon terminals in the PBL^{Oprm1} neurons (Figure 3C) and observed eGFP signals from their terminals in the preBötC (Figure 3D). To functionally characterize this circuit, we expressed hM3Dq or control eYFP in the PBL^{Oprm1} neurons and activated their axon terminals in the preBötC by stereotaxically injecting the potent hM3Dq-receptor agonist clozapine (Gomez et al., 2017) directly into the preBötC to facilitate immediate hM3Dq activation (Figure 3F). Stimulation of PBL^{Oprm1}-preBötC terminals in this manner significantly increased breathing rate (Figures 3E and 3G). Collectively, these results indicate that PBL^{Oprm1} neurons can regulate breathing behaviors by conveying signals from the forebrain, hindbrain, and limbic areas to preBötC rhythm-generating neurons.

Noxious stimuli simultaneously increase breathing rate and PBL^{Oprm1} activity

Noxious and anxiogenic stimuli can elevate breathing rhythm in humans (Bass and Gardner, 1985; Jafari et al., 2017). To investigate this phenomenon in mice, we measured breathing in awake mice while challenging the animals with a noxious stimulus, electric foot shock, and two anxiogenic conditions, the elevated plus maze (EPM) and elevated platform. We found that foot-shock-induced breathing changes depended upon basal breathing state and stimulus strength. When mild foot shocks (0.04 mA, 2 s) were administered to well-habituated mice with low baseline breathing rates, mice displayed an immediate increase in breathing rate as well as locomotor activity (Figure S4A). However, when stronger foot shocks typically used in fear conditioning (0.2 mA, 2 s) were administered to well-habituated mice, mice displayed an initial increase in breathing rate followed by a marked decrease while switching from a stationary pose to a hectic running and jumping behavior (Figure S4B). When the same magnitude of foot shock (0.2 mA, 2 s) was administered to unhabituated mice with high baseline breathing rates, mice immediately decreased their breathing rate and initiated running and jumping behavior (Figure S4C). These different breathing responses to foot shock suggest that pain-induced breathing change is influenced by multiple factors: the baseline breathing rate, the intensity of the noxious stimuli, and the animal's locomotor activity. During EPM assay, breathing rate decreased as mice exited the open arm and increased as they entered the open arm (Figures S4D and S4E). To minimize the involvement of locomotor activity while monitoring anxiety-induced changes in breathing, we placed the animals on an elevated circular platform (10 cm diameter, 100 cm elevated from the floor), which increased the breathing rate and plethysmograph amplitude compared to the home cage (Figures S4F–S4H). These data suggest that affective states and breathing behaviors are tightly correlated in mice.

Because PBL^{Oprm1} neurons receive monosynaptic inputs from the brain areas that mediate pain perception (Figures 3A, 3B, and S3C), they may also be actively involved in breathing increases induced by pain. To explore this possibility, we monitored breathing and PBL^{Oprm1} activity simultaneously during noxious stimulus presentation in both anesthetized and awake mice. In anesthetized mice, we recorded breathing with piezoelectric sensors and calcium signals with fiber photometry (Figures 4A and 4F).

(I and K) Activating PBL^{Oprm1} neurons via ChR2 significantly increased breathing rate (n = 8, I) while inhibiting PBL^{Oprm1} neurons via ArchT significantly decreased breathing rate (n = 8, K). These effects were not observed in controls (n = 8 for I and n = 7 for K).

(J) Representative traces of voltage, breathing rate (range 52.3–201.9 bpm), and plethysmograph amplitude (range 4.3–12.7 mV) during optogenetic stimulation (blue shade, 10 s).

(L) Representative traces of voltage, breathing rate (range 84.5–122.6 bpm), and plethysmograph amplitude (range 6.6–8.6 mV) during optogenetic inhibition (yellow shade, 5 s).

(M and O) Representative traces depicting frequency-dependent photostimulation effects (M) or intensity-dependent photoinhibition effects (O) on breathing rate. Scale, 100 bpm/5 s (M) or 10 bpm/2 s (O).

(N and P) Quantification of average breathing rate during the light-on period in (M) and (O), normalized to pre-stimulation baseline (n = 4 for N and n = 3 for P). Statistical analyses were performed using two-way ANOVA analysis with Bonferroni's multiple comparison post hoc test (C, E, I, and K) and one-way ANOVA with Tukey's post hoc test, comparing each frequency with the no-stimulation control group (N and P), *p < 0.05; **p < 0.01; ***p < 0.001; ****p < 0.0001. Data are presented as mean ± SEM. See also Figure S2.

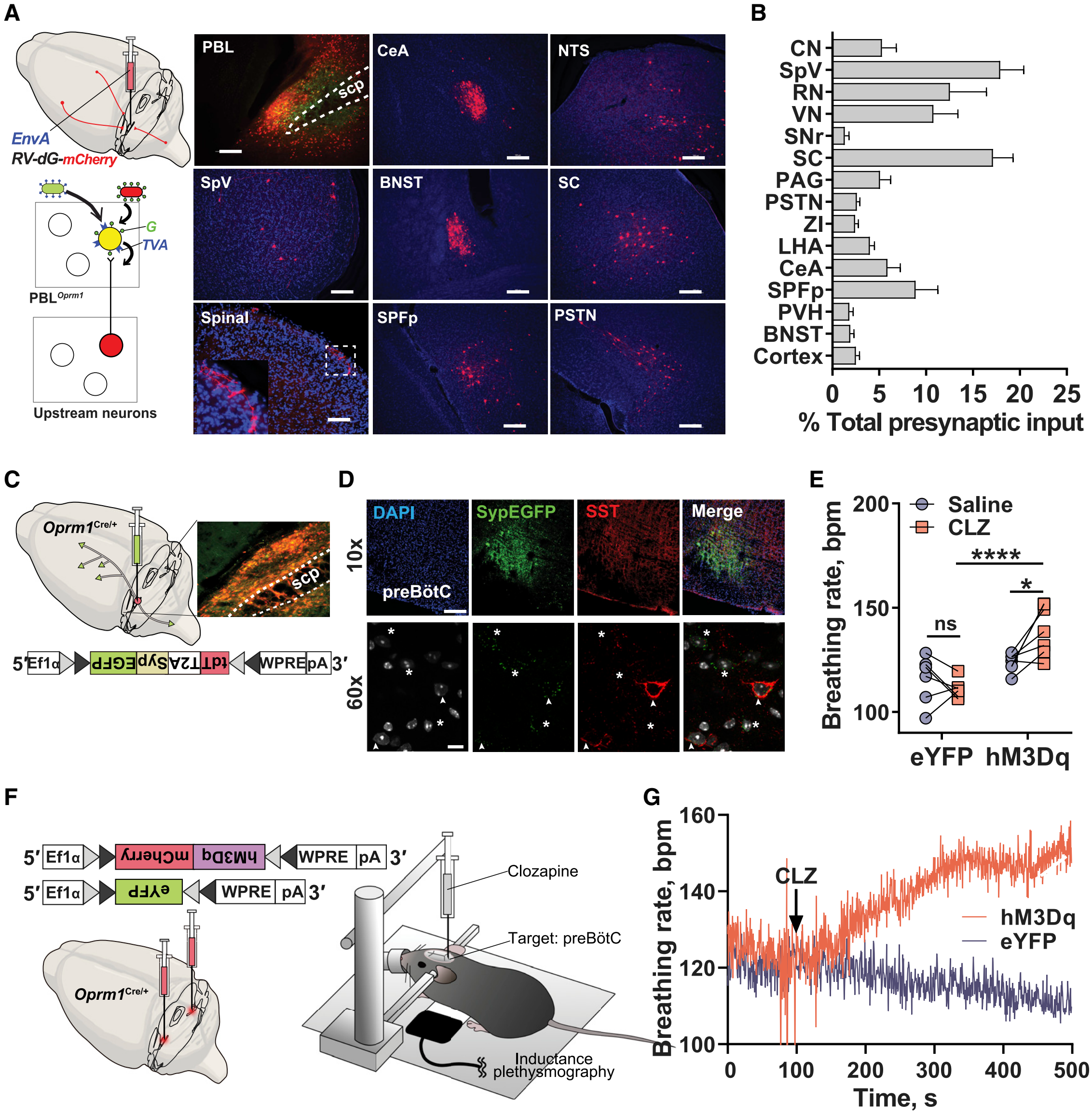

Figure 3. Input-output mapping of PBL^{Oprm1} neural connections

(A) Schematic of monosynaptic retrograde tracing from PBL^{Oprm1} neurons and representative images of the starter region and upstream areas. SpV, spinal trigeminal nucleus; Spinal, spinal cord dorsal horn; CeA, central amygdalar nucleus; BNST, bed nuclei of the stria terminalis; SPFp, subparafascicular nucleus, parvicellular part; NTS, nucleus tractus solitarius; SC, superior colliculus; PSTN, parasubthalamic nucleus. Scale, 100 μm (spinal) or 200 μm (others).

(B) Quantification of the presynaptic inputs (n = 7). CN, cochlear nucleus; RN, reticular nucleus; VN, vestibular nucleus; SNr, substantia nigra, reticular part; PAG, periaqueductal gray; ZI, zona incerta; LHA, lateral hypothalamic area; PVH, paraventricular hypothalamic nucleus.

(C) Schematic and histology of nucleus-targeting tdTomato and axon-targeting synaptophysin:eGFP expression in PBL^{Oprm1} neurons.

(D) Coronal sections showing PBL^{Oprm1} axon terminals in the preBötC marked by SST immunohistochemistry. Arrowheads and asterisks denote SST$^+$ and SST$^-$ preBötC neurons that receive PBL^{Oprm1} inputs. Scale, 200 μm (10 ×) or 10 μm (60 ×).

(E and G) Clozapine injection into preBötC increased breathing rate in hM3Dq-expressing animals (n = 7) but not in eYFP-expressing animals (n = 6, E). Representative traces are shown in (G). Statistical analyses were performed using two-way ANOVA analysis with Bonferroni's multiple comparison post hoc test, $^*p < 0.05$; $^{****}p < 0.0001$.

(F) Schematic of chemogenetic terminal stimulation of hM3Dq-expressing PBL^{Oprm1} neurons by stereotaxic injection of clozapine (CLZ, 200 nL, 1 μg/mL) into preBötC of anesthetized mice. Data are presented as mean ± SEM. See also Figure S3.

We challenged the animals with noxious thermal stimuli by touching the tail with a hot rod (55°C) (Figure 4A) and observed an immediate increase in breathing rate (Figures 4B and 4C), plethysmograph amplitude (Figures S4I and S4J), and PBL^{Oprm1} activity (Figures 4D and 4E). Noxious mechanical stimuli (tail pinch with 300 g pressure) (Figure 4F) also robustly increased breathing rate (Figures 4G and 4H), plethysmograph amplitude (Figures S4K and S4L), and calcium signals (Figures 4I and 4J).

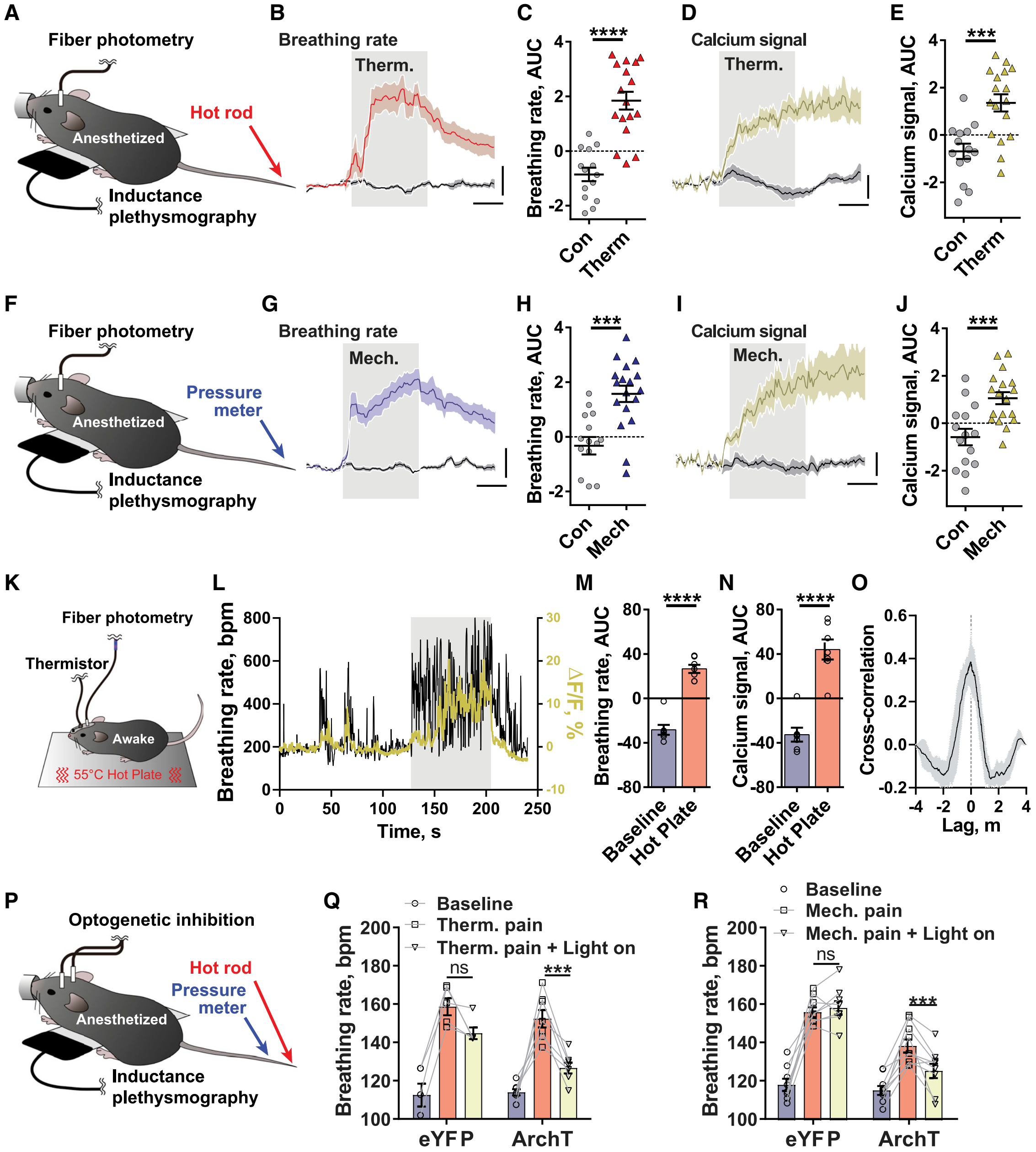

Figure 4. PBL^{Oprm1} neurons are recruited during pain-induced hyperventilation

(A and F) Schematic of simultaneous monitoring of PBL^{Oprm1} activity and breathing rate in anesthetized mice during noxious thermal (55°C hot rod, A) and mechanical (tail pinch with 300 g pressure, F) stimulation.

(B, D, G, and I) Average traces of normalized breathing rate (B and G) and PBL^{Oprm1} activity (D and I) before and after applying thermal (B and D) and mechanical (G and I) noxious or control stimuli (thermal control, a room-temperature rod; mechanical control, gentle touch) (gray shade) (B and D: n = 14–17 traces from 7 mice; G and I: n = 15–18 traces from 7 mice). Scale, 2 s/10 bpm (B), 2 s/2% ΔF/F (D), 1 s/10 bpm (G), 1 s/2% ΔF/F (I).

(C, E, H, and J) Thermal (Therm) or mechanical (Mech) stimulation significantly increased the areas under the curve (AUCs) of the breathing rate (C and H) and calcium activity (E and J) compared to control (Con) stimulation.

(K and L) Schematic (K) and representative traces (L) of simultaneous monitoring of PBL^{Oprm1} activity and breathing rate in freely moving mice during noxious thermal stimulus presentation (gray shade in L depicts changing the temperature from 25°C to 55°C).

(M and N) Thermal pain increased AUCs of breathing rate (M) and calcium (N) traces compared to baseline (n = 7).

(O) Breathing rate and calcium signals displayed strong cross-correlation during thermal pain stimulation (n = 7).

(P) Schematic of inhibiting PBL^{Oprm1} neurons during thermal and mechanical stimulation.

(Q and R) Inhibiting PBL^{Oprm1} neurons by ArchT attenuated hyperventilation evoked by thermal (Q) and mechanical (R) pain signals (n = 13 stimulations from 3 mice), which was not observed in the eYFP group (n = 9 stimulations from 3 mice).

(legend continued on next page)

Next, we delivered the noxious thermal stimulus to freely moving mice by first habituating them on a room-temperature metal plate and then increasing the surface temperature to 55°C (Figure 4K). We observed dramatic increases in breathing rate (Figures 4L–4N), plethysmograph amplitude (Figures S4M and S4N), and calcium signals, as well as tight correlations of calcium signals with both breathing rate (Figure 4O) and amplitude (Figure S4O). These data indicate that PBL^{Oprm1} neurons are strongly activated by painful stimuli and exhibit dynamics that closely resemble breathing across a broad range of physiological conditions.

Since inhibiting PBL^{Oprm1} neurons decreased breathing, we tested whether doing so could also override pain-induced hyperventilation. Therefore, we optogenetically silenced PBL^{Oprm1} neurons in anesthetized mice with ArchT and monitored breathing rhythm after applying noxious stimuli (Figure 4P). Optogenetic PBL^{Oprm1} inhibition significantly attenuated thermal (Figure 4Q) and mechanical (Figure 4R) pain-induced increases in breathing rate but did not affect the control group. These results indicate that silencing PBL^{Oprm1} neurons can counteract pain-induced hyperventilation, possibly by lowering baseline breathing rate (Figure 2) or blocking stimulus-evoked breathing changes (Jiang et al., 2004).

PBL^{Oprm1} inhibition alleviates affective pain and anxiety-like behaviors

Because PBL^{Oprm1} neurons reciprocally project to pain and emotional processing areas such as the CeA and BNST (Figures 3A, 3B, S3C, and S3D), we hypothesized that they also mediate pain perception and anxiety-like behaviors. However, inhibiting PBL^{Oprm1} neurons by hM4Di did not alter thermal or mechanical pain sensitivity, as measured by paw withdrawal latencies in hot plate (Figures 5A and 5B) and von Frey tests (Figures 5D and 5E). These results are consistent with a recent report that parabrachial manipulation did not alter baseline pain sensitivity (Chiang et al., 2020). However, these hM4Di animals showed a longer latency to jump (Figure 5C), suggesting reduced motivation to escape from the hot plate, which implies a lower level of affective-motivation pain (Han et al., 2015).

To further assess affective-motivational pain perception, we performed the formalin test (Figure 5F), which evaluates chemical and inflammatory pain by measuring biphasic licking responses to formalin injection during the first and second inflammatory phases (Le Bars et al., 2001). The first acute phase is mediated by direct stimulation of the nociceptors, while the second inflammatory phase is modulated by areas that process affective pain (Huang et al., 2006; Vaccarino and Melzack, 1989). Compared to controls, hM4Di-expressing mice displayed attenuated paw-licking behaviors in the second, but not the first, phase, indicating that chemogenetic inhibition of PBL^{Oprm1} neurons reduced affective pain, but not detection of the peripheral stimulus (Figures 5G and S5A–S5E). We also performed contextual fear conditioning tests to further evaluate the affective pain response (Figure 5H). In classical Pavlovian fear conditioning, the unpleasantness of foot-shock-induced acute pain drives the animal to display defensive responses and associate specific cues or contexts with fear; thus, the freezing behavior during and after conditioning correlate with the affective aspect of pain. hM4Di mice displayed less freezing than controls in both conditioning (Figure 5I) and the fear memory retrieval phase (Figure 5J). Together, these results indicate that inhibiting PBL^{Oprm1} neurons attenuates affective pain perception without altering sensory pain perception.

To further examine the role of PBL^{Oprm1} neurons in mediating negative affect, we first performed the EPM test to test anxiety-like behaviors. The hM4Di-expressing group spent a significantly longer time in the open arms (Figures 5K–5M), visited open arms more frequently (Figure S5F), and traveled longer distances (Figure S5G) compared to the control group, indicating that PBL^{Oprm1} neurons are also involved in mediating anxiety. Next, to test whether PBL^{Oprm1} neurons encode positive or negative valence, we performed real-time place preference and aversion (RTPP and RTPA) tests with ArchT (Figures 5N–5P) or ChR2 (Figures 5Q–5S) optogenetics. ArchT-expressing mice stayed significantly longer in the "light-on" chamber compared to the "light-off chamber," whereas the control group spent equal time in both chambers (Figure 5P). Although we observed apnea in some anesthetized mice following repeated optogenetic inhibition (Figure S2M), we did not observe it in mice during the behavioral test, likely because of the different baseline breathing rates between awake (300–600 bpm) and anesthetized animals (<100 bpm). Conversely, the ChR2-expressing mice displayed avoidance behavior toward the "light-on" chamber (Figure 5S). Overall, these results indicate that PBL^{Oprm1} inactivation alleviated affective pain and anxiety-like behavior while encoding positive valence, whereas PBL^{Oprm1} activation contributed to pain-induced hyperventilation and encoded negative valence.

Single PBL^{Oprm1} neurons respond to both breathing and pain

It is possible that a homogeneous PBL^{Oprm1} population may regulate both breathing and pain or, alternatively, that heterogeneous subpopulations of PBL^{Oprm1} neurons may independently regulate these behaviors. To test these possibilities, we first investigated the molecular heterogeneity of PBL^{Oprm1} neurons. We performed RNAscope *in situ* hybridization for *Oprm1* and seven known markers of the dorsal (PBdl) and external lateral PB (PBel), namely, the *Calca*, *Tac1*, *Nts*, *Htr2a*, *FoxP2*, *Pdyn*, and *Tacr1* genes, many of which have been reported to mediate pain and breathing behaviors, such as escape and hypercapnic arousal (Barik et al., 2018; Chiang et al., 2020; Deng et al., 2020; Han et al., 2015; Kaur et al., 2020). *Oprm1* transcripts were found in both the PBdl and PBel, exhibiting 10%–40% co-localization with each marker gene tested (Figures S6A and S6B).

Since PBL^{Oprm1} neurons are molecularly heterogenous, we performed miniscope single-cell calcium imaging to compare

---

Statistical analyses were performed using two-way ANOVA analysis with Bonferroni's multiple comparison post hoc test (Q and R), two-tailed unpaired t test (C, E, H, and J), and two-tailed paired t test (M and N). Ns, not significant; *p < 0.05; ***p < 0.001; ****p < 0.0001. Data are presented as mean ± SEM. See also Figure S4.

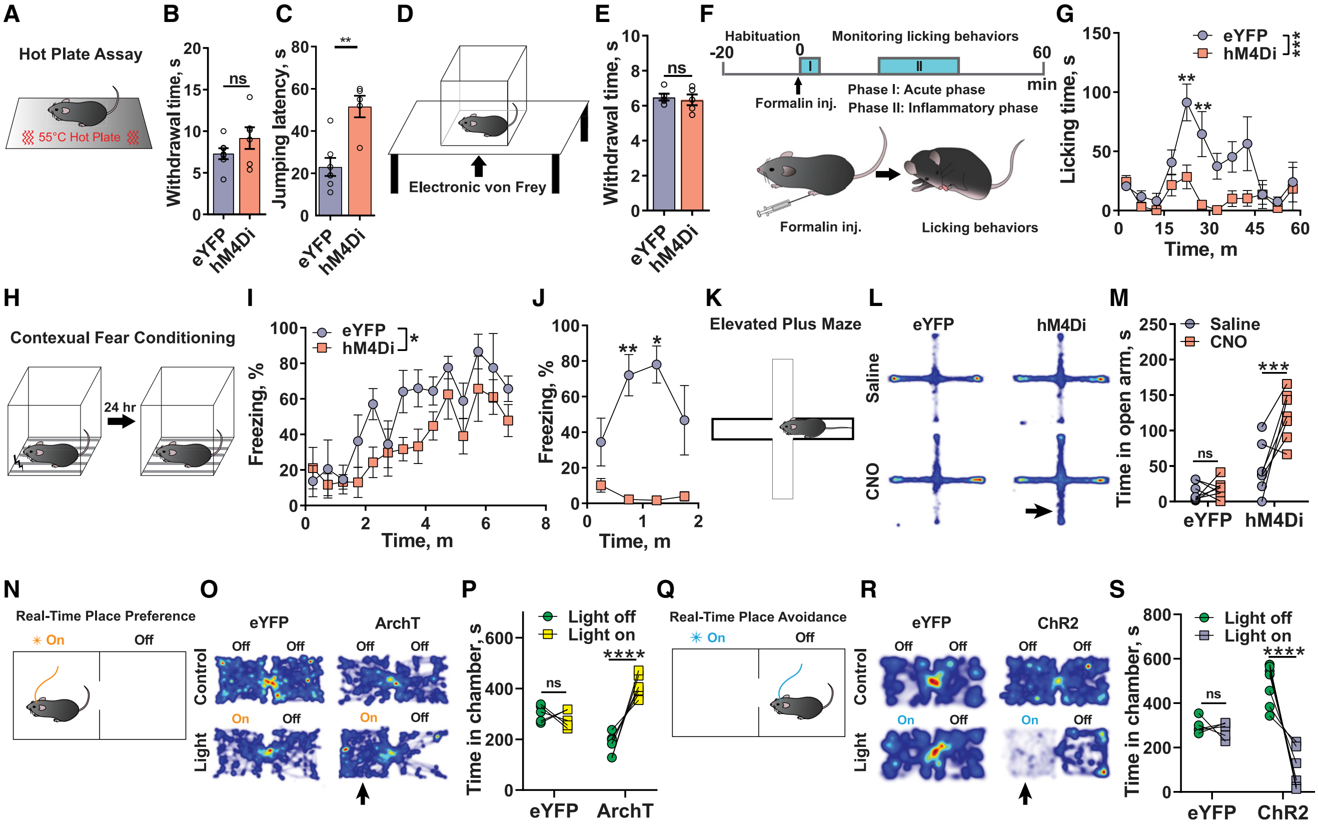

Figure 5. PBL^{Oprm1} inhibition alleviates affective pain perception and attenuates anxiety-like behaviors

(A and D) Schematic of hot plate assay for testing thermal sensitivity and nocifensive behavior (A) and electronic von Frey assay for testing mechanical sensitivity (D).

(B and E) CNO injection (7.5 mg/kg i.p., same as below) did not result in differences in thermal (B) or mechanical (E) sensitivity in mice expressing hM4Di (n = 5) or eYFP (n = 7 for B, n = 5 for E) in PBL^{Oprm1} neurons.

(C) Mice expressing hM4Di (n = 5) in PBL^{Oprm1} neurons displayed a longer latency to jump when stimulated with a von Frey fiber after CNO injection compared to the eYFP group (n = 7).

(F) Schematic of formalin assay for chemical and inflammatory sensitivity test.

(G) CNO injection significantly reduced paw-licking time in hM4Di group (n = 5) compared to eYFP controls (n = 7).

(H) Schematic of contextual fear conditioning test, in which CNO was injected before the conditioning session.

(I) CNO injection significantly decreased freezing behavior in the hM4Di group compared to the eYFP group during conditioning (5 0.2 mA, 2 s foot shocks, uneven inter-shock intervals) (n = 5 per group).

(J) CNO injection significantly decreased freezing behavior in the hM4Di group compared to eYFP controls during the contextual retrieval test 24 h after conditioning (n = 5 per group).

(K) Schematic of EPM assay for testing anxiety-like behavior.

(L) Heatmaps of averaged movement in each group during the EPM test. Arrow denotes open arm.

(M) The hM4Di group, but not the eYFP group, increased open arm time after CNO injection compared to saline injection (n = 7 per group).

(N and Q) Schematics of real-time place preference (RTPP, N) and avoidance (RTPA, Q) tests.

(O and R) Heatmaps of averaged movement in each group during RTPP (O) and RTPA (R) tests.

(P and S) Mice expressing ArchT in PBL^{Oprm1} neurons (n = 6) spent significantly more time in the “light-on” chamber compared to the eYFP group (n = 6, P), whereas mice expressing ChR2 (n = 8) spent significantly less time in the “light-on” chamber compared to the controls (n = 5, S).

Statistical analyses were performed using two-way ANOVA analysis with Bonferroni’s multiple comparison post hoc test (G, I, J, M, P, and S) or two-tailed unpaired t test (B, C, and E). Ns, not significant; $^{*}p < 0.05$; $^{**}p < 0.01$; $^{***}p < 0.001$; $^{****}p < 0.0001$. Data are presented as mean ± SEM. See also Figure S5.

the responses of individual PBL^{Oprm1} neurons to breathing and pain (pinching) in the same animal (Figure 6A). Many neurons displayed activities correlated with breathing (Figure 6B) and pinching (Figure 6C). Among 108 cells recorded, 62.0% responded to both breathing and pain (Figures 6D and 6E), 14.8% responded to breathing only (Figure 6F), and 21.3% responded only to pinching (Figure 6G). These results indicate that the majority of the PBL^{Oprm1} neurons are recruited by both breathing and pain behaviors.

Two distinct PBL^{Oprm1} subpopulations diverge to emotion-processing and breathing centers

PBL^{Oprm1} neurons project to many areas, including medullary breathing centers and limbic regions that process pain and

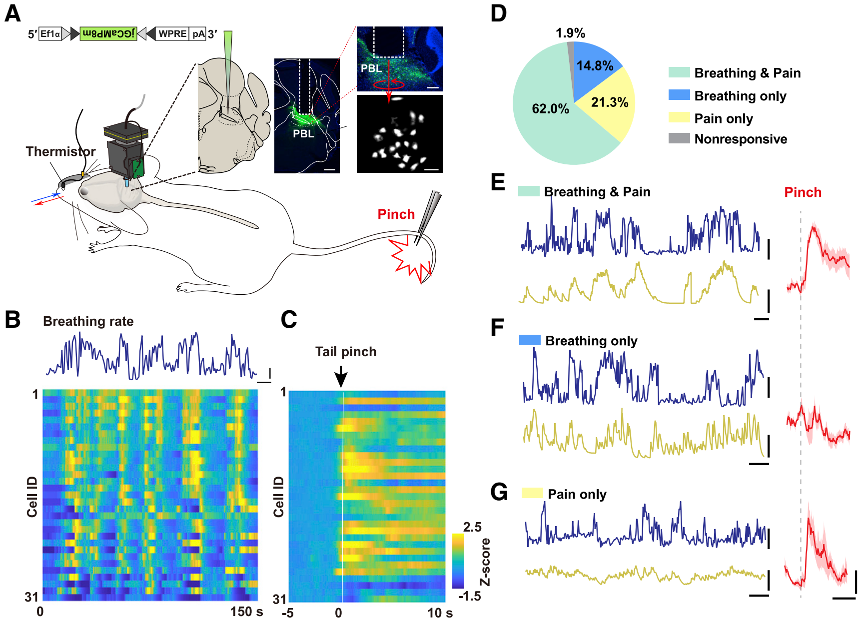

Figure 6. Same PBL^{Oprm1} neurons regulate breathing and pain

(A) Schematic of simultaneous recording of breathing and calcium activity from single PBL^{Oprm1} neurons with a microendoscope. Tail pinching represents noxious stimuli. Scale, 500 μm (4×)/200 μm (10×)/100 μm (region of interest [ROI]).

(B) Example trace of the breathing rate (top) and heatmaps of individual neuronal activities (bottom) demonstrating their synchronization. Scale, 100 bpm/10 s.

(C) Heatmap of individual neuronal activities aligned at the onset of pinching (white line). Each row in (B) and (C) corresponds to the same neuron from one representative mouse.

(D) Pie chart showing the percentage of neurons that respond to breathing only (16/108), pain only (23/108), both (67/108), and neither (2/108, from 5 mice).

(E–G) Example breathing rate and calcium traces (left) and averaged pinching response (right) for an example neuron that showed responses to both breathing and pinching (E), breathing only (F), and pain only (G). Scale, left panel: 200 bpm (top), 20 (E)/3 (F)/1 (G) units of *Z* scored ΔF/F/20 s; right panel: 1 unit of *Z* scored ΔF/F/5 s. Data are presented as mean ± SEM. See also Figure S6.

emotion (Figures S3C and S3D). To determine whether single PBL^{Oprm1} neurons collaterally project to both areas or two different subpopulations divergently project to each area, we performed projection-specific anatomical tracing using intersectional viral approaches. First, we injected retrogradely transported AAVs Cre-dependently encoding mCherry into the CeA of *Oprm1*$^{Cre/+}$ mice to label CeA-projecting PBL^{Oprm1} neurons (*Oprm1*$^{PBL \rightarrow CeA}$ neurons) with mCherry. In the same animals, we then injected retrograde AAVs encoding Cre-dependent codon-optimized FLP-recombinase (FLPo) into the preBötC and FLP-dependent ChR2-eYFP into the PBL to label preBötC-projecting PBL^{Oprm1} neurons (*Oprm1*$^{PBL \rightarrow preBötC}$ neurons) with eYFP (Figure 7A). Interestingly, these two subpopulations were anatomically segregated. The CeA-projecting neurons were clustered in the PBel while the preBötC-projectors were localized to the surrounding central lateral (PBcl), lateral crescent (PBlc), and the ventral PBel regions, together forming a "core-shell" like structure (Figures 7B, S7A, and S7B) with little overlap (Figure 7C). Although the PBel and PBlc have previously been distinguished based on projection patterns (Chamberlin and Saper, 1992; Herbert et al., 1990; Yokota et al., 2015), this distinctive core-shell pattern at the same coronal and horizontal levels has not been previously reported. Moreover, the core (*Oprm1*$^{PBL \rightarrow CeA}$) and shell (*Oprm1*$^{PBL \rightarrow preBötC}$) neurons projected to largely non-overlapping downstream regions. The core neurons projected to forebrain areas including the BNST and the intralaminar nucleus (ILN), while the shell neurons extensively projected to hindbrain areas, including the caudal pontine reticular nucleus (PnC), retrotrapezoid nucleus (RTN), NTS, spinal vestibular nucleus (SpIV), and spinal trigeminal nucleus (SpV) (Figures S7C and S7D). These results imply that the core and shell neurons may exert different functions via projections to the forebrain and the hindbrain, respectively.

Core and shell PBL^{Oprm1} neurons differentially regulate breathing, pain, and anxiety

To test whether core and shell PBL^{Oprm1} subpopulations are differentially involved in breathing and pain regulation, we first simultaneously monitored the activities and breathing of each subpopulation (Figures 7D and 7I). The activities of both core and shell neurons were tightly correlated with breathing rate (Figures 7E, 7F, 7J, and 7K) and plethysmograph amplitude (Figures S7E, S7F, S7L, and S7M). Moreover, the breathing rhythm and the activities of each population increased concurrently upon delivery of noxious thermal (Figures 7G, 7L, S7G, S7H, S7N, and S7O) and mechanical stimuli (same stimuli as in Figure 4) (Figures S7I–S7K and S7P–S7R) in anesthetized mice. Interestingly, breathing rate changes during sniffing events were correlated with activity of shell, but not core, neurons (Figures 7H and 7M). These results indicate that the core and shell neurons are differentially involved in regulating breathing rhythm.

We then performed projection-specific manipulation experiments to investigate the roles of each subpopulation in regulating breathing, affective pain perception, and anxiety-like behaviors by expressing ChR2 and hM4Di in each population using intersectional viral tools (Figures 8A and 8F). ChR2-mediated stimulation of core neurons significantly increased breathing rate (Figure 8B), number of jumps on the hot plate (Barik et al., 2018; Han et al., 2015) (Figure 8C), and paw-licking behavior during the inflammatory phase of the formalin assay (Figures S8A–S8C). To examine negative affective behaviors, we performed the EPM, RTPA, and open field freezing tests while activating the core neurons. Compared to controls, animals expressing ChR2 in the core neurons avoided the light-paired chamber in the RTPA test (Figure 8D), spent significantly less time in the open arm during the EPM test (Figure 8E), and displayed freezing behaviors in the open field arena when given repeated photostimulation

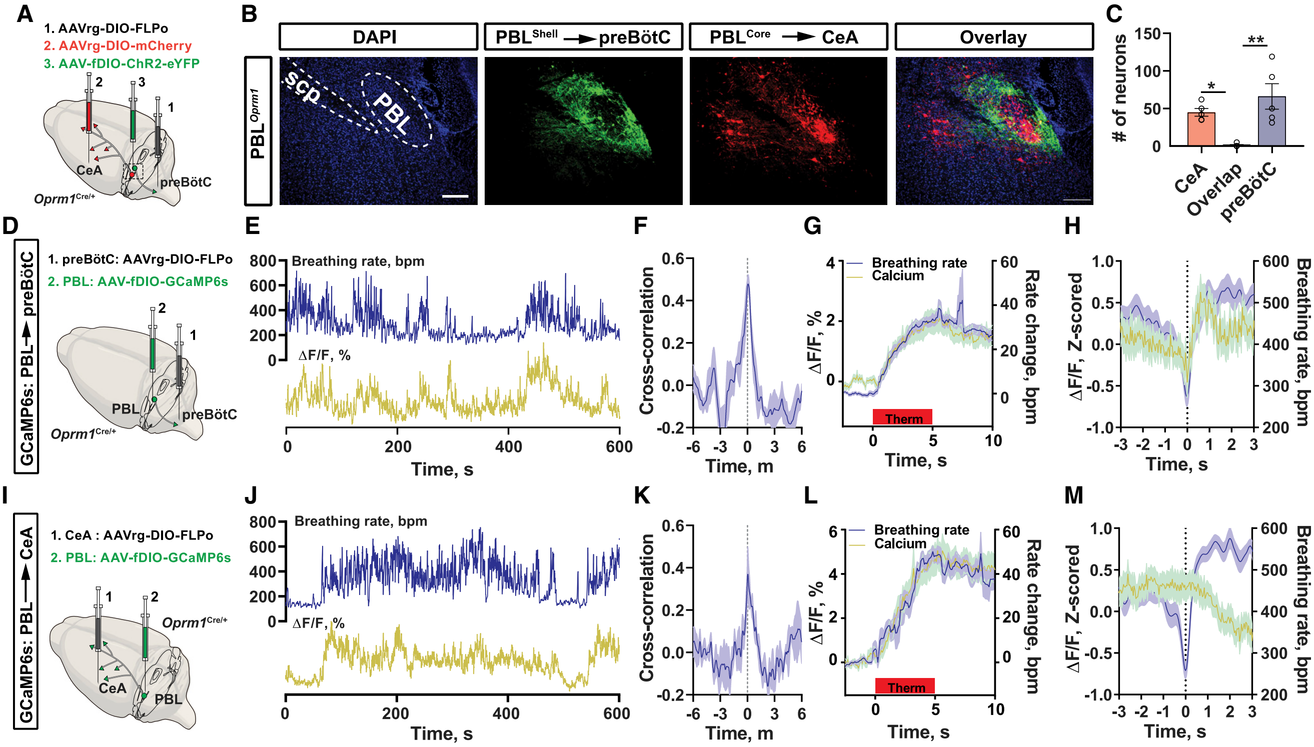

Figure 7. PBL^{Oprm1} subpopulations projecting to the CeA and the preBötC form a "core-shell" pattern and are differentially involved in breathing regulation

(A) Schematic of projection-specific retrograde labeling strategy.

(B) Representative images of preBötC-projecting (eYFP-expressing, green, "shell") and CeA-projecting PBL^{Oprm1} neurons (mCherry-expressing, red, "core").

(C) Quantification of labeled core and shell neurons and their overlap (n = 5 animals). Statistical analyses were performed using one-way ANOVA analysis with Tukey's multiple comparison post hoc test. $^{*}p < 0.05$; $^{**}p < 0.01$.

(D and I) Viral strategy for subpopulation-specific activity monitoring of shell (D) and core (I) neurons.

(E and J) Both shell (E) and core (J) neurons displayed activities tightly correlated with breathing. Calcium signal ranges, shell: −4.1% to 20.6%; core: −7.7% to 41.7%.

(F and K) Both shell (F) and core (K) activities strongly correlated with breathing rate (n = 4).

(G and L) Both shell (G) and core (L) activities and breathing rate were increased by nociceptive thermal stimulation (n = 15–21 trials from 5–7 animals for each group).

(H and M) Activities from shell neurons (H), but not core (M) neurons, tightly correlated with breathing during rearing-sniffing events (n = 25–35 trials from 3 mice for each group). Data are presented as mean ± SEM. See also Figure S7.

(Figure S8D). Similar to the core neurons, photostimulation of shell neurons not only elevated breathing rate (Figure 8G) but also exacerbated affective pain perception (Figure 8H for hot plate and S8E–S8G for formalin assay) and promoted behaviors associated with negative affect (Figure 8I for RTPA, 8J for EPM, and S8H for freezing).

For loss-of-function experiments, we inhibited each subpopulation with hM4Di (Runegaard et al., 2018) (Figures 8K and 8P). Chemogenetic inhibition of core neurons not only significantly reduced baseline breathing rate (Figure 8L) but also markedly alleviated affective pain perception (Figures 8M, S8I–S8M for formalin assay, and 8N for hot plate assay) and anxiety responses (Figure 8O for EPM, and S8N and S8O for open field test). Chemogenetic inhibition of shell neurons also decreased baseline breathing rate (Figure 8Q) but did not affect affective pain responses (Figures 8R and S8P–S8T for formalin assay, Figure 8S for hot plate assay) or anxiety-like behaviors (Figure 8T for EPM and Figures S8U and S8V for open field test) as in the core neurons. These results indicate that both core and shell neurons actively regulate breathing and affective behaviors such as pain and anxiety, but at different levels. Both the core and shell neurons are indispensable for regulating breathing. The core neurons are sufficient and necessary for regulating affective pain and anxiety-like behaviors, whereas the shell neurons are only sufficient but not required for these behaviors.

To test whether shell neurons are necessary for pain-induced breathing increase, if not the pain response itself, we again chemogenetically inhibited the shell neurons and then measured pain-induced breathing changes during the formalin assay (Figure S8W). During the acute pain period, both the hM4Di and eYFP animals displayed similar levels of dynamic breathing rate changes accompanying excessive licking behaviors (Figure S8X). However, only the eYFP group displayed a breathing

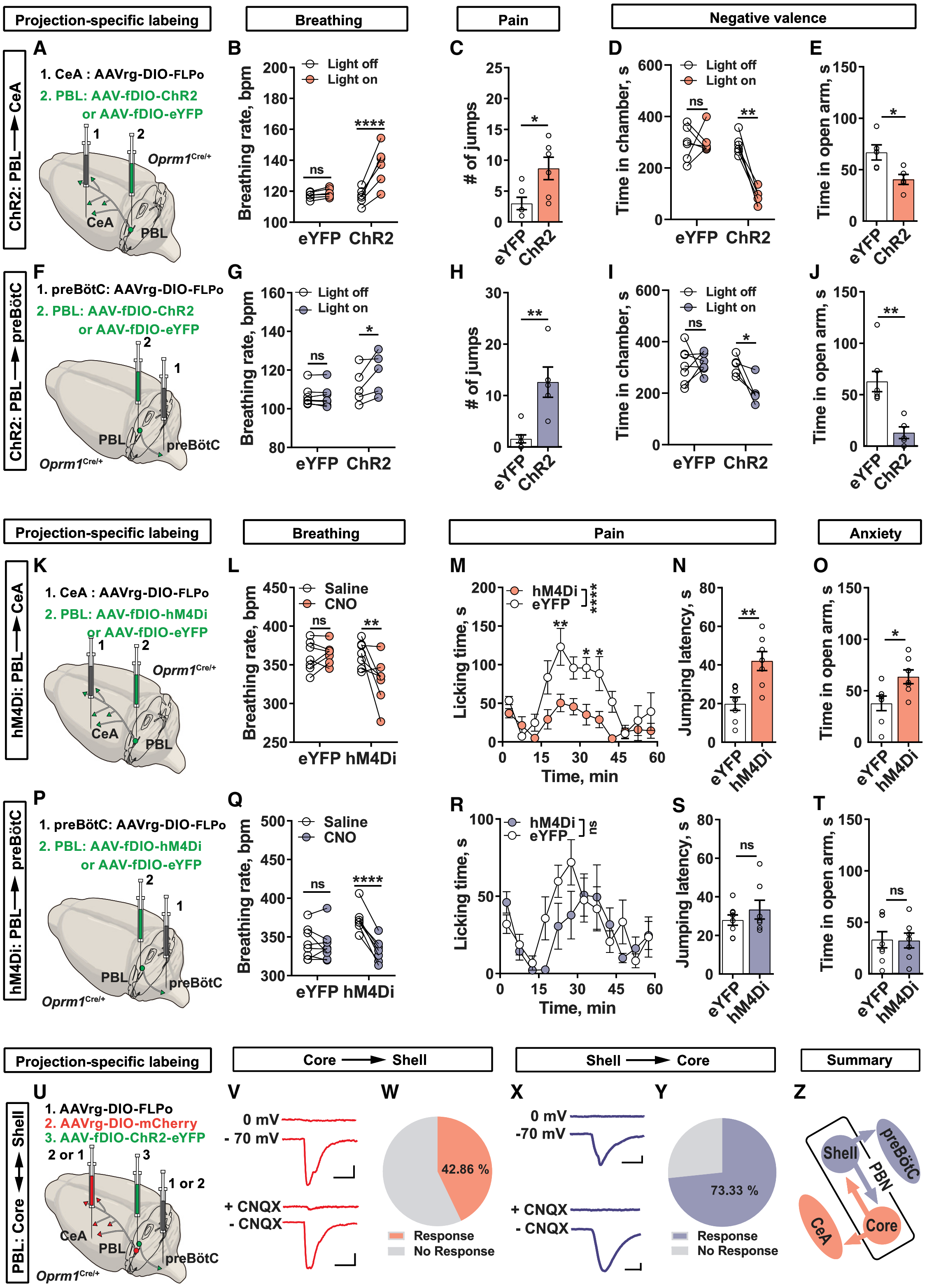

(legend on next page)

rate increase during the inflammatory pain phase (Figure S8Y). These results indicate that the shell neurons are required to regulate pain-induced breathing changes, as well as basal breathing rhythm.

PBL^{Oprm1} subpopulations send excitatory inputs to each other

Inhibiting the PBL^{Oprm1} subpopulations resulted in different outcomes in pain and anxiety, yet optogenetic stimulation of both subpopulations induced the same phenotype. We therefore wondered if the PBL^{Oprm1} subpopulations reciprocally interact with each other. To explore this possibility, we performed projection-specific *ex vivo* whole-cell patch-clamp electrophysiological recording using the same intersectional approach described above (Figure 7A) to record one subpopulation expressing mCherry while stimulating the other subpopulation via ChR2 (Figure 8U). Photostimulation of the core neurons evoked excitatory postsynaptic currents (oEPSCs) in 42.86% of the shell neurons (Figure 8W), and stimulating the shell neurons evoked oEPSC in 73.33% of the core neurons (Figure 8Y). Moreover, we observed that both responses were glutamatergic because no inhibitory postsynaptic current was detected by photostimulation, and the application of the AMPA receptor antagonist CNQX abolished all oEPSCs (Figures 8V and 8X). Our data suggest that PBL^{Oprm1} neurons integrate breathing with pain and anxiety via a reciprocally connected excitatory network of core and shell subpopulations that divergently project to the CeA and the preBötC (Figure 8Z).

DISCUSSION

By combining cell-type- and projection-specific circuit dissection tools with respiratory monitoring approaches, we identify the PBL^{Oprm1} neurons that simultaneously regulate breathing and negative affect through two anatomically distinct but interconnected core and shell subpopulations that diverge to the limbic and medullary breathing areas. We also find that these core and shell subpopulations are reciprocally interconnected with excitatory synapses to collectively regulate breathing, pain, and anxiety-like behaviors. Together, these data provide a circuit-based mechanism of coordinating breathing with pain and emotions.

Our results demonstrate that PBL^{Oprm1} neurons consist of two non-overlapping subpopulations with a "core-shell" configuration determined by divergent projections to the CeA and preBötC. Both the core $Oprm1^{\mathrm{PBL}\rightarrow\mathrm{CeA}}$ and shell $Oprm1^{\mathrm{PBL}\rightarrow\mathrm{preB\ddot{o}tC}}$ neurons directly regulate breathing rhythm, but only the shell neurons are involved in behaviorally entrained breathing behaviors such as sniffing, indicating that these two subpopulations play different roles in breathing regulation. These results are in line with previous reports implicating the existence of the PBL → preBötC breathing circuit (Chamberlin and Saper, 1992; Ellenberger and Feldman, 1990; Fulwiler and Saper, 1984; Herbert et al., 1990) and the involvement of CeA in breathing regulation (Frysinger et al., 1988; Nobis et al., 2018; Yang et al., 2020).

Our results also show that the core $Oprm1^{\mathrm{PBL}\rightarrow\mathrm{CeA}}$ and shell $Oprm1^{\mathrm{PBL}\rightarrow\mathrm{preB\ddot{o}tC}}$ neurons are differentially involved in regulating pain perception. Optogenetic stimulation of both the core and shell populations exacerbated affective pain and negative emotional behaviors. Chemogenetic inhibition of core neurons substantially attenuates the behaviors associated with affective pain and negative emotions, but these behaviors were unaltered by chemogenetic inhibition of the shell neurons. These results indicate that the core and shell subpopulations are differentially involved in regulating negative affect (e.g., affective pain and anxiety).

Based on these results, we speculate that the dynamic interplays of breathing and negative affect, such as pain-induced hyperventilation (Jafari et al., 2017), hyperventilation during panic attack (Bass and Gardner, 1985), or exacerbated negative affect by voluntary hyperventilation (Hornsveld et al., 1995; Lum, 1981), can be mediated by the recurrent excitatory connection between core and shell PBL^{Oprm1} neurons and their differential involvement in regulating pain and breathing. However, it should be noted that breathing and negative affect do not always influence each other. For example, a rapid increase of breathing induced by emotionally neutral behaviors, such as sniffing and exercise, does not recruit changes in negative affect. Reciprocally connected core-shell PBL^{Oprm1} neurons may not be involved in these conditions. Instead, shell neurons that do not make

Figure 8. PBL^{Oprm1} subpopulations differentially regulate breathing and pain

(A and F) Schematic of projection-specific optogenetic activation of core (A) and shell (F) subpopulations.

(B–E and G–J) Upon light stimulation, animals expressing ChR2 in core (B–E) and shell (G–J) neurons increased breathing rate (B and G), completed more jumps during the hot plate test (C and H), spent less time in the light-paired chamber in the RTPA test (D and I), and spent less time in the open arm of the EPM (E and J) compared with eYFP controls (core: ChR2/eYFP, n = 6/6; shell: ChR2/eYFP, n = 5/7).

(K and P) Schematic for projection-specific chemogenetic inhibition of the core (K) and shell (P) subpopulations.

(L–O) Upon CNO injection (5 mg/kg i.p.), animals expressing hM4Di in core neurons decreased breathing rate (L), decreased licking time in the formalin assay (M), increased latency to the first jump in the hot plate test (N), and increased time spent in the open arm of the EPM (O) compared to the eYFP controls (hM4Di/eYFP, n = 7/7).

(Q–T) Upon CNO injection, animals expressing hM4Di in shell neurons decreased breathing rate (Q), but did not change licking time in the formalin assay (R), latency to the first jump in the hot plate test (S), or time spent in the open arm of the EPM (T) compared to the eYFP controls (hM4Di/eYFP, n = 8/7).

(U) Schematic for projection-specific electrophysiology. Whole-cell patch-clamp recording was performed with one subpopulation expressing mCherry, while blue light was delivered to stimulate the other subpopulation expressing ChR2 under the control of retrogradely transported FLPo.

(V and X) Example EPSC traces in shell (V) and core (X) neurons evoked by 2 ms blue light stimulation of the other subpopulation, before and after CNQX application. Scale, 20 ms/20 pA (V and X, top); 10 ms/20 pA (X, bottom).

(W and Y) Percentage of shell (W, n = 14) and core (Y, n = 15) neurons displaying light-evoked EPSC responses.

(Z) Summary of the inter- and extra-PBL^{Oprm1} circuits that collectively regulate breathing, pain, and anxiety.

Statistical analyses were performed using two-way ANOVA analysis with Bonferroni's multiple comparison post hoc test (B, D, G, I, L, M, Q, and R) or two-tailed unpaired t test (C, E, H, J, N, O, S, and T). Ns, not significant; *$p < 0.05$; **$p < 0.01$; ****$p < 0.0001$. Data are presented as mean ± SEM. See also Figure S8.

synapse onto the core neurons, possibly the “breathing only” population in Figure 6, may be actively involved in these conditions. Indeed, the shell neurons, not core neurons, are highly correlated with breathing during exploratory sniffing (Figures 7H and 7M). Moreover, chemogenetic inhibition of core neurons, not shell neurons, reduced affective pain and anxiety (Figure 8). These results suggest that inputs inhibiting PBL^{Oprm1} neurons can alleviate negative affect only by acting upon the core neurons. These results also imply that the hypoalgesia caused by controlled slow breathing likely requires the recruitment of the cortex or limbic system (Jafari et al., 2017) and is not driven by inhibiting the shell *Oprm1*$^{\mathrm{PBL}\rightarrow\mathrm{preB\ddot{o}tC}}$ neurons.

PBL^{Oprm1} neurons receive monosynaptic inputs from a broad array of sensory and limbic areas and in turn relay this information to both the breathing and affective pain networks through the core and shell neurons (Figure S8Z). Notably, the core and shell neurons form a recurrent excitatory network, which is uniquely positioned to converge brain-wide top-down and bottom-up inputs and collectively controls breathing and internal affective states. Furthermore, these inputs are not limited to pain or anxiety but can be expanded to a broader range, such as visceral or gustatory inputs relayed by the NTS (Duschek et al., 2013), which is reciprocally connected with the PBL^{Oprm1} neurons (Figures 4 and S4).

The fact that the PBL^{Oprm1} neurons regulate pain and breathing also explains why opioids can simultaneously inhibit both pain and breathing, manifested as opioid analgesia and OIRD. Indeed, PBL^{Oprm1} inhibition caused by excessive opioids is one of the neural mechanisms of OIRD (Liu et al., 2021). The endogenous opioid system in the PBL has been less explored, however. Possible upstream sources of endogenous opioids in the PBL include proopiomelanocortin (*Pomc*) neurons in the NTS (Wang et al., 2015), proenkephalin (*Penk*) neurons in the CeA (Kim et al., 2017), and prodynorphin (*Pdyn*) and *Penk* neurons in the PB (Norris et al., 2021). Future studies exploring the modulation of PBL^{Oprm1} neurons by these endogenous opioids are needed to understand the endogenous roles of PBL^{Oprm1} neurons as the converging hub of emotional, sensory, and physiological functions.

STAR★METHODS

Detailed methods are provided in the online version of this paper and include the following:

- KEY RESOURCES TABLE
- RESOURCE AVAILABILITY
    - ○ Lead contact
    - ○ Materials availability
    - ○ Data and code availability
- EXPERIMENTAL MODEL AND SUBJECT DETAILS
    - ○ Mouse lines
- METHOD DETAILS
    - ○ Respiratory measurements
    - ○ Stereotaxic surgery
    - ○ Fiber photometry
    - ○ Single-cell calcium imaging
    - ○ Convergent cross-mapping
    - ○ Chemogenetics
    - ○ *Ex vivo* electrophysiology
    - ○ Optogenetics
    - ○ Histology
    - ○ Immunohistochemistry
    - ○ RNA *in situ* hybridization
    - ○ Imaging
    - ○ Monosynaptic rabies tracing
    - ○ Subpopulation-specific anatomical mapping
    - ○ Elevated plus maze test
    - ○ Hot plate test
    - ○ Electronic von Frey test
    - ○ Formalin test
    - ○ Contextual fear conditioning
    - ○ Open field test
    - ○ Freezing measurement
    - ○ Breathing measurement with pain or anxiety tests
- QUANTIFICATION AND STATISTICAL ANALYSIS

SUPPLEMENTAL INFORMATION

Supplemental information can be found online at https://doi.org/10.1016/j.neuron.2021.11.029.

ACKNOWLEDGMENTS

We thank the Han lab members for the critical discussion of the paper, Dr. Jane Chen for the technical support of Miniscope calcium imaging, and Benjamin Roberts for the stylistic editing of the manuscript. S.H. is supported by 1R01MH116203 from NIMH and a Brain Research Foundation Fay/Frank Seed Grant. S.L. is supported by the Salk Women & Science Special Award, the Mary K. Chapman Foundation, and the Jesse & Caryl Philips Foundation. This work is supported by the Waitt Advanced Biophotonics Core Facility of the Salk Institute with funding from NIH-NCI CCSG: P30 014195 and the Waitt Foundation.

AUTHOR CONTRIBUTIONS

S.H. conceived the idea, designed and constructed the respiratory monitoring apparatus, and secured funding. S.H. and S.L. designed the experiments and wrote the manuscript. S.L. performed most of the experiments. M.Y. contributed to the electrophysiology and whole-population RTPP and RTPA experiments. G.M.P. performed the CCM analysis. J.J. contributed to the figure illustrations. S.M.S. and H.J. contributed to the rabies tracing and histology experiments. J.K. contributed to the projection-specific electrophysiology experiment. H.J. and S.J.K. contributed to the formalin experiment.

DECLARATION OF INTERESTS

The authors declare no competing interests.

INCLUSION AND DIVERSITY

We worked to ensure sex balance in the selection of non-human subjects. One or more of the authors of this paper self-identifies as an underrepresented ethnic minority in science. One or more of the authors of this paper received support from a program designed to increase minority representation in science. While citing references scientifically relevant for this work, we also actively worked to promote gender balance in our reference list.

Received: February 26, 2021
Revised: September 8, 2021
Accepted: November 20, 2021
Published: December 17, 2021

REFERENCES

Abrams, D.J., Zheng, L., Choo, K.S., Yang, J.J., Wei, W., Anchordoquy, T.J., Zawia, N.H., and Stevens, K.E. (2008). An initial animal proof-of-concept study for central administration of clozapine to schizophrenia patients. Schizophr. Res. *100*, 86–96.

Ashhad, S., and Feldman, J.L. (2020). Emergent elements of inspiratory rhythmogenesis: network synchronization and synchrony propagation. Neuron *106*, 482–497.e4.

Bachmutsky, I., Wei, X.P., Kish, E., and Yackle, K. (2020). Opioids depress breathing through two small brainstem sites. eLife *9*, e52694.

Barik, A., Thompson, J.H., Seltzer, M., Ghitani, N., and Chesler, A.T. (2018). A Brainstem-Spinal Circuit Controlling Nocifensive Behavior. Neuron *100*, 1491–1503.e3.

Bass, C., and Gardner, W. (1985). Emotional influences on breathing and breathlessness. J. Psychosom. Res. *29*, 599–609.

Bautista, T.G., Sun, Q.-J., and Pilowsky, P.M. (2014). The generation of pharyngeal phase of swallow and its coordination with breathing: interaction between the swallow and respiratory central pattern generators. Prog. Brain Res. *212*, 253–275.

Biskamp, J., Bartos, M., and Sauer, J.-F. (2017). Organization of prefrontal network activity by respiration-related oscillations. Sci. Rep. *7*, 45508.

Boiten, F.A., Frijda, N.H., and Wientjes, C.J.E. (1994). Emotions and respiratory patterns: review and critical analysis. Int. J. Psychophysiol. *17*, 103–128.

Callaway, E.M., and Luo, L. (2015). Monosynaptic Circuit Tracing with Glycoprotein-Deleted Rabies Viruses. J. Neurosci. *35*, 8979–8985.

Chamberlin, N.L. (2004). Functional organization of the parabrachial complex and intertrigeminal region in the control of breathing. Respir. Physiol. Neurobiol. *143*, 115–125.

Chamberlin, N.L., and Saper, C.B. (1992). Topographic organization of cardiovascular responses to electrical and glutamate microstimulation of the parabrachial nucleus in the rat. J. Comp. Neurol. *326*, 245–262.

Chamberlin, N.L., and Saper, C.B. (1994). Topographic organization of respiratory responses to glutamate microstimulation of the parabrachial nucleus in the rat. J. Neurosci. *14*, 6500–6510.

Chamberlin, N.L., Mansour, A., Watson, S.J., and Saper, C.B. (1999). Localization of mu-opioid receptors on amygdaloid projection neurons in the parabrachial nucleus of the rat. Brain Res. *827*, 198–204.

Chen, T.-W., Wardill, T.J., Sun, Y., Pulver, S.R., Renninger, S.L., Baohan, A., Schreiter, E.R., Kerr, R.A., Orger, M.B., Jayaraman, V., et al. (2013). Ultrasensitive fluorescent proteins for imaging neuronal activity. Nature *499*, 295–300.

Chiang, M.C., Nguyen, E.K., Canto-Bustos, M., Papale, A.E., Oswald, A.-M.M., and Ross, S.E. (2020). Divergent neural pathways emanating from the lateral parabrachial nucleus mediate distinct components of the pain response. Neuron *106*, 927–939.e5.

Chow, B.Y., Han, X., Dobry, A.S., Qian, X., Chuong, A.S., Li, M., Henninger, M.A., Belfort, G.M., Lin, Y., Monahan, P.E., and Boyden, E.S. (2010). High-performance genetically targetable optical neural silencing by light-driven proton pumps. Nature *463*, 98–102.

Chow, B.Y., Han, X., and Boyden, E.S. (2012). Genetically encoded molecular tools for light-driven silencing of targeted neurons. Prog. Brain Res. *196*, 49–61.

Cohen, M.I. (1971). Switching of the respiratory phases and evoked phrenic responses produced by rostral pontine electrical stimulation. J. Physiol. *217*, 133–158.

Cui, Y., Kam, K., Sherman, D., Janczewski, W.A., Zheng, Y., and Feldman, J.L. (2016). Defining preBötzinger Complex Rhythm- and Pattern-Generating Neural Microcircuits In Vivo. Neuron *91*, 602–614.

Dahan, A., Sarton, E., Teppema, L., Olievier, C., Nieuwenhuijs, D., Matthes, H.W., and Kieffer, B.L. (2001). Anesthetic potency and influence of morphine and sevoflurane on respiration in mu-opioid receptor knockout mice. Anesthesiology *94*, 824–832.

Dana, H., Sun, Y., Mohar, B., Hulse, B.K., Kerlin, A.M., Hasseman, J.P., Tsegaye, G., Tsang, A., Wong, A., Patel, R., et al. (2019). High-performance calcium sensors for imaging activity in neuronal populations and microcompartments. Nat. Methods *16*, 649–657.

Del Negro, C.A., Funk, G.D., and Feldman, J.L. (2018). Breathing matters. Nat. Rev. Neurosci. *19*, 351–367.

Deng, J., Zhou, H., Lin, J.-K., Shen, Z.-X., Chen, W.-Z., Wang, L.-H., Li, Q., Mu, D., Wei, Y.-C., Xu, X.-H., and Sun, Y.G. (2020). The Parabrachial Nucleus Directly Channels Spinal Nociceptive Signals to the Intralaminar Thalamic Nuclei, but Not the Amygdala. Neuron *107*, 909–923.e6.

Deyle, E.R., and Sugihara, G. (2011). Generalized theorems for nonlinear state space reconstruction. PLoS ONE *6*, e18295.

Dick, T.E., Dutschmann, M., Feldman, J.L., Fong, A.Y., Hülsmann, S., Morris, K.M., Ramirez, J.M., and Smith, J.C.; Respiratory Neurobiology Consortium (2018). Facts and challenges in respiratory neurobiology. Respir. Physiol. Neurobiol. *258*, 104–107.

Duschek, S., Werner, N.S., and Reyes Del Paso, G.A. (2013). The behavioral impact of baroreflex function: a review. Psychophysiology *50*, 1183–1193.

Dutschmann, M., and Dick, T.E. (2012). Pontine mechanisms of respiratory control. Compr. Physiol. *2*, 2443–2469.

Dutschmann, M., and Herbert, H. (2006). The Kölliker-Fuse nucleus gates the postinspiratory phase of the respiratory cycle to control inspiratory off-switch and upper airway resistance in rat. Eur. J. Neurosci. *24*, 1071–1084.

Ellenberger, H.H., and Feldman, J.L. (1990). Brainstem connections of the rostral ventral respiratory group of the rat. Brain Res. *513*, 35–42.

Feleky, A. (1916). The influence of the emotions on respiration. J. Exp. Psychol. *1*, 218–241.

Fenno, L.E., Mattis, J., Ramakrishnan, C., Hyun, M., Lee, S.Y., He, M., Tucciarone, J., Selimbeyoglu, A., Berndt, A., Grosenick, L., et al. (2014). Targeting cells with single vectors using multiple-feature Boolean logic. Nature Methods *11*, 763–772.

Fraser, A.M., and Swinney, H.L. (1986). Independent coordinates for strange attractors from mutual information. Phys. Rev. A Gen. Phys. *33*, 1134–1140.

Frysinger, R.C., Zhang, J.X., and Harper, R.M. (1988). Cardiovascular and respiratory relationships with neuronal discharge in the central nucleus of the amygdala during sleep-waking states. Sleep *11*, 317–332.

Fulwiler, C.E., and Saper, C.B. (1984). Subnuclear organization of the efferent connections of the parabrachial nucleus in the rat. Brain Res. *319*, 229–259.

Gauriau, C., and Bernard, J.-F. (2002). Pain pathways and parabrachial circuits in the rat. Exp. Physiol. *87*, 251–258.

Gomez, J.L., Bonaventura, J., Lesniak, W., Mathews, W.B., Sysa-Shah, P., Rodriguez, L.A., Ellis, R.J., Richie, C.T., Harvey, B.K., Dannals, R.F., et al. (2017). Chemogenetics revealed: DREADD occupancy and activation via converted clozapine. Science *357*, 503–507.

Han, X., Chow, B., Zhou, H., Klapoetke, N., Chuong, A., Rajimehr, R., Yang, A., Baratta, M., Winkle, J., Desimone, R., et al. (2011). A High-Light Sensitivity Optical Neural Silencer: Development and Application to Optogenetic Control of Non-Human Primate Cortex. Frontiers in Systems Neuroscience *5*, 18.

Han, S., Soleiman, M.T., Soden, M.E., Zweifel, L.S., and Palmiter, R.D. (2015). Elucidating an Affective Pain Circuit that Creates a Threat Memory. Cell *162*, 363–374.

Herbert, H., Moga, M.M., and Saper, C.B. (1990). Connections of the parabrachial nucleus with the nucleus of the solitary tract and the medullary reticular formation in the rat. J. Comp. Neurol. *293*, 540–580.

Hornsveld, H., Garssen, B., and van Spiegel, P. (1995). Voluntary hyperventilation: the influence of duration and depth on the development of symptoms. Biol. Psychol. *40*, 299–312.

Huang, J., Chang, J.-Y., Woodward, D.J., Baccalá, L.A., Han, J.-S., Wang, J.-Y., and Luo, F. (2006). Dynamic neuronal responses in cortical and thalamic areas during different phases of formalin test in rats. Exp. Neurol. *200*, 124–134.

Jafari, H., Courtois, I., Van den Bergh, O., Vlaeyen, J.W.S., and Van Diest, I. (2017). Pain and respiration: a systematic review. Pain *158*, 995–1006.

Janak, P.H., and Tye, K.M. (2015). From circuits to behaviour in the amygdala. Nature *517*, 284–292.

Jiang, M., Alheid, G.F., Calandriello, T., and McCrimmon, D.R. (2004). Parabrachial-lateral pontine neurons link nociception and breathing. Respir. Physiol. Neurobiol. *143*, 215–233.

Kaur, S., De Luca, R., Khanday, M.A., Bandaru, S.S., Thomas, R.C., Broadhurst, R.Y., Venner, A., Todd, W.D., Fuller, P.M., Arrigoni, E., and Saper, C.B. (2020). Role of serotonergic dorsal raphe neurons in hypercapnia-induced arousals. Nat. Commun. *11*, 2769.

Kim, J., Zhang, X., Muralidhar, S., LeBlanc, S.A., and Tonegawa, S. (2017). Basolateral to Central Amygdala Neural Circuits for Appetitive Behaviors. Neuron *93*, 1464–1479.e5.

Kravitz, A.V., and Kreitzer, A.C. (2012). Striatal mechanisms underlying movement, reinforcement, and punishment. Physiology (Bethesda) *27*, 167–177.

Le Bars, D., Gozariu, M., and Cadden, S.W. (2001). Animal models of nociception. Pharmacol. Rev. *53*, 597–652.

Levitt, E.S., Abdala, A.P., Paton, J.F., Bissonnette, J.M., and Williams, J.T. (2015). μ opioid receptor activation hyperpolarizes respiratory-controlling Kölliker-Fuse neurons and suppresses post-inspiratory drive. J. Physiol. *593*, 4453–4469.

Li, P., Janczewski, W.A., Yackle, K., Kam, K., Pagliardini, S., Krasnow, M.A., and Feldman, J.L. (2016). The peptidergic control circuit for sighing. Nature *530*, 293–297.

Liu, S., Kim, D.-I., Oh, T.G., Pao, G.M., Kim, J.-H., Palmiter, R.D., Banghart, M.R., Lee, K.-F., Evans, R.M., and Han, S. (2021). Neural basis of opioid-induced respiratory depression and its rescue. Proc. Natl. Acad. Sci. USA *118*, 23.

Lum, L. (1981). Hyperventilation and anxiety state (London, England: SAGE Publications Sage UK).

Mahn, M., Saraf-Sinik, I., Patil, P., Pulin, M., Bitton, E., Karalis, N., Bruentgens, F., Palgi, S., Gat, A., Dine, J., et al. (2021). Efficient optogenetic silencing of neurotransmitter release with a mosquito rhodopsin. Neuron *109*, 1621–1635.e8.

Matthes, H.W., Maldonado, R., Simonin, F., Valverde, O., Slowe, S., Kitchen, I., Befort, K., Dierich, A., Le Meur, M., Dollé, P., et al. (1996). Loss of morphine-induced analgesia, reward effect and withdrawal symptoms in mice lacking the mu-opioid-receptor gene. Nature *383*, 819–823.

McAfee, S.S., Ogg, M.C., Ross, J.M., Liu, Y., Fletcher, M.L., and Heck, D.H. (2016). Minimally invasive highly precise monitoring of respiratory rhythm in the mouse using an epithelial temperature probe. J. Neurosci. Methods *263*, 89–94.

Moberly, A.H., Schreck, M., Bhattarai, J.P., Zweifel, L.S., Luo, W., and Ma, M. (2018). Olfactory inputs modulate respiration-related rhythmic activity in the prefrontal cortex and freezing behavior. Nat. Commun. *9*, 1528.

Montandon, G., Qin, W., Liu, H., Ren, J., Greer, J.J., and Horner, R.L. (2011). PreBotzinger complex neurokinin-1 receptor-expressing neurons mediate opioid-induced respiratory depression. J. Neurosci. *31*, 1292–1301.

Moore, J.D., Deschênes, M., Furuta, T., Huber, D., Smear, M.C., Demers, M., and Kleinfeld, D. (2013). Hierarchy of orofacial rhythms revealed through whisking and breathing. Nature *497*, 205–210.

Mortola, J.P., and Frappell, P.B. (1998). On the barometric method for measurements of ventilation, and its use in small animals. Can. J. Physiol. Pharmacol. *76*, 937–944.

Navarrete-Opazo, A.A., Cook-Snyder, D.R., Miller, J.R., Callison, J.J., McCarthy, N., Palkovic, B., Stuth, E.A.E., Zuperku, E.J., and Stucke, A.G. (2020). Endogenous glutamatergic inputs to the Parabrachial Nucleus/Kölliker-Fuse Complex determine respiratory rate. Respir. Physiol. Neurobiol. *277*, 103401.

Nguyen Chi, V., Müller, C., Wolfenstetter, T., Yanovsky, Y., Draguhn, A., Tort, A.B., and Brankačk, J. (2016). Hippocampal respiration-driven rhythm distinct from theta oscillations in awake mice. J. Neurosci. *36*, 162–177.

Nobis, W.P., Schuele, S., Templer, J.W., Zhou, G., Lane, G., Rosenow, J.M., and Zelano, C. (2018). Amygdala-stimulation-induced apnea is attention and nasal-breathing dependent. Ann. Neurol. *83*, 460–471.

Norris, A.J., Shaker, J.R., Cone, A.L., Ndiokho, I.B., and Bruchas, M.R. (2021). Parabrachial opioidergic projections to preoptic hypothalamus mediate behavioral and physiological thermal defenses. eLife *10*, e60779.

Oh, S.W., Harris, J.A., Ng, L., Winslow, B., Cain, N., Mihalas, S., Wang, Q., Lau, C., Kuan, L., Henry, A.M., et al. (2014). A mesoscale connectome of the mouse brain. Nature *508*, 207–214.

Osakada, F., Mori, T., Cetin, A.H., Marshel, J.H., Virgen, B., and Callaway, E.M. (2011). New Rabies Virus Variants for Monitoring and Manipulating Activity and Gene Expression in Defined Neural Circuits. Neuron *71*, 617–631.

Palmiter, R.D. (2018). The Parabrachial Nucleus: CGRP Neurons Function as a General Alarm. Trends Neurosci. *41*, 280–293.

Pautrat, A., Rolland, M., Barthelemy, M., Baunez, C., Sinniger, V., Piallat, B., Savasta, M., Overton, P.G., David, O., and Coizet, V. (2018). Revealing a novel nociceptive network that links the subthalamic nucleus to pain processing. eLife *7*, e36607.

Prkic, I., Mustapic, S., Radocaj, T., Stucke, A.G., Stuth, E.A., Hopp, F.A., Dean, C., and Zuperku, E.J. (2012). Pontine μ-opioid receptors mediate bradypnea caused by intravenous remifentanil infusions at clinically relevant concentrations in dogs. J. Neurophysiol. *108*, 2430–2441.

Runegaard, A.H., Sørensen, A.T., Fitzpatrick, C.M., Jørgensen, S.H., Petersen, A.V., Hansen, N.W., Weikop, P., Andreasen, J.T., Mikkelsen, J.D., Perrier, J.-F., et al. (2018). Locomotor- and reward-enhancing effects of cocaine are differentially regulated by chemogenetic stimulation of Gi-signaling in dopaminergic neurons. eNeuro *5*, ENEURO.0345–17.2018.

Sahibzada, N., Dean, P., and Redgrave, P. (1986). Movements resembling orientation or avoidance elicited by electrical stimulation of the superior colliculus in rats. J. Neurosci. *6*, 723–733.

Saper, C.B., and Loewy, A.D. (1980). Efferent connections of the parabrachial nucleus in the rat. Brain Res. *197*, 291–317.

Smith, J.C., Ellenberger, H.H., Ballanyi, K., Richter, D.W., and Feldman, J.L. (1991). Pre-Bötzinger complex: a brainstem region that may generate respiratory rhythm in mammals. Science *254*, 726–729.

Smotherman, M., Schwartz, C., and Metzner, W. (2010). Vocal–respiratory interactions in the parabrachial nucleus. In Handbook of Behavioral Neuroscience, S.M. Brudzynski, ed. (Elsevier), pp. 383–392.

Stujenske, J.M., Spellman, T., and Gordon, J.A. (2015). Modeling the spatiotemporal dynamics of light and heat propagation for in vivo optogenetics. Cell Rep. *12*, 525–534.

Sugihara, G., and May, R.M. (1990). Nonlinear forecasting as a way of distinguishing chaos from measurement error in time series. Nature *344*, 734–741.

Sugihara, G., May, R., Ye, H., Hsieh, C.H., Deyle, E., Fogarty, M., and Munch, S. (2012). Detecting causality in complex ecosystems. Science *338*, 496–500.

Tan, W., Pagliardini, S., Yang, P., Janczewski, W.A., and Feldman, J.L. (2010). Projections of preBötzinger complex neurons in adult rats. J. Comp. Neurol. *518*, 1862–1878.

Vaccarino, A.L., and Melzack, R. (1989). Analgesia produced by injection of lidocaine into the anterior cingulum bundle of the rat. Pain *39*, 213–219.

Varga, A.G., Reid, B.T., Kieffer, B.L., and Levitt, E.S. (2020). Differential impact of two critical respiratory centres in opioid-induced respiratory depression in awake mice. J. Physiol. *598*, 189–205.

Wang, S.C., Ngai, S.H., and Frumin, M.J. (1957). Organization of central respiratory mechanisms in the brain stem of the cat: genesis of normal respiratory rhythmicity. Am. J. Physiol. *190*, 333–342.

Wang, D., He, X., Zhao, Z., Feng, Q., Lin, R., Sun, Y., Ding, T., Xu, F., Luo, M., and Zhan, C. (2015). Whole-brain mapping of the direct inputs and axonal projections of POMC and AgRP neurons. Front. Neuroanat. *9*, 40.

Whitney, H. (1936). The imbedding of manifolds in families of analytic manifolds. Ann. Math. *37*, 865–878.

Yang, C.F., Kim, E.J., Callaway, E.M., and Feldman, J.L. (2020). Monosynaptic projections to excitatory and inhibitory preBötzinger complex neurons. Front. Neuroanat. *14*, 58.

Yokota, S., Kaur, S., VanderHorst, V.G., Saper, C.B., and Chamberlin, N.L. (2015). Respiratory-related outputs of glutamatergic, hypercapnia-responsive parabrachial neurons in mice. J. Comp. Neurol. *523*, 907–920.

Zhang, Y., Rózsa, M., Bushey, D., Zheng, J., Reep, D., Liang, Y., Broussard, G.J., Tsang, A., Tsegaye, G., Patel, R., et al. (2020). jGCaMP8 Fast Genetically Encoded Calcium Indicators. Janelia Research Campus, https://doi.org/10.25378/janelia.13148243.v4.

Zhang, F., Wang, L.-P., Brauner, M., Liewald, J.F., Kay, K., Watzke, N., Wood, P.G., Bamberg, E., Nagel, G., Gottschalk, A., and Deisseroth, K. (2007). Multimodal fast optical interrogation of neural circuitry. Nature *446*, 633–639.

Zingg, B., Chou, X., Zhang, Z., Mesik, L., Liang, F., Tao, H.W., and Zhang, L.I. (2017). AAV-Mediated Anterograde Transsynaptic Tagging: Mapping Corticocollicular Input-Defined Neural Pathways for Defense Behaviors. Neuron *93*, 33–47.

STAR★METHODS

KEY RESOURCES TABLE

REAGENT or RESOURCE	SOURCE	IDENTIFIER
Antibodies		
Rabbit anti-somatostatin-14 (1:250)	Peninsula Laboratories International	RRID: AB_518614
Goat anti-choline acetyltransferase (1:100)	Sigma-Aldrich	RRID: AB_2079751
Rabbit anti-mu opioid receptor (1:250)	ImmunoStar	RRID: AB_572251
Cy™3 AffiniPure Donkey Anti-Rabbit IgG (H+L) (1:500)	Jackson ImmunoResearch Laboratories	RRID: AB_2307443
Alexa Fluor® 647 AffiniPure Donkey Anti-Goat IgG (H+L) (1:500)	Jackson ImmunoResearch Laboratories	RRID: AB_2340436
Alexa Fluor® 647 AffiniPure Donkey Anti-Rabbit IgG (H+L) (1:300)	Jackson ImmunoResearch Laboratories	RRID: AB_2492288
Bacterial and virus strains		
AAV1-syn-FLEX-jGCaMP7s-WPRE	Dana et al., 2019	Addgene viral prep # 104491-AAV1
AAV1-Syn-GCaMP6f-WPRE-SV40	Chen et al., 2013	Addgene viral prep # 100837-AAV1
AAV2-EF1a-DIO-eYFP	Karl Deisseroth	Addgene plasmid # 27056
AAVDJ-EF1a-DIO-hM3D(Gq)-mCherry	Bryan Roth, Salk Institute Viral Vector Core	Addgene plasmid # 50460
AAVDJ-EF1a-DIO-hM4D(Gi)-mCherry	Bryan Roth, Salk Institute Viral Vector Core	Addgene plasmid # 50461
AAVDJ-EF1a-DIO-hChR2(H134R)-EYFP-WPRE-pA	Karl Deisseroth, Salk Institute Viral Vector Core	Addgene plasmid # 20298
AAVDJ-FLEX-ArchT-GFP	Han et al., 2011, Salk Institute Viral Vector Core	Addgene plasmid # 28307
AAV8-hSyn-FLEX-TVA-P2A-GFP-2A-oG	John Naughton, Salk Institute Viral Vector Core	Addgene plasmid # 85225
EnvA G-Deleted Rabies-mCherry	Osakada et al., 2011, Salk Institute Viral Vector Core	Addgene plasmid # 32636
AAV2-phSyn1(S)-FLEX-tdTomato-T2A-SypEGFP-WPRE	Oh et al., 2014, Salk Institute Viral Vector Core	Addgene plasmid # 51509
AAVrg-EF1a-DIO-FLPo-WPRE-hGHpA	Zingg et al., 2017, Salk Institute Viral Vector Core	Addgene plasmid # 87306
AAVrg-EF1a-DIO-mCherry	Bryan Roth, Salk Institute Viral Vector Core	Addgene plasmid # 50462
AAV8-Ef1a-fDIO-GCaMP6s	Rylan Larsen, Salk Institute Viral Vector Core	Addgene plasmid # 105714
AAV9-EF1a-fDIO-hChR2(H134R)-EYFP	Fenno et al., 2014, Salk Institute Viral Vector Core	Addgene plasmid # 55639
AAV8-EF1a-fDIO-EYFP	Fenno et al., 2014, Salk Institute Viral Vector Core	Addgene plasmid # 55641
AAVDJ-hSyn-fDIO-hM4D(Gi)-mCherry-WPREpA	Runegaard et al., 2018	Addgene plasmid # 154867
AAV8-hSyn-DO-GCaMP6m	Karl Deisseroth, UNC Viral Vector Core	N/A
AAVDJ-syn-FLEX-jGCaMP8m-WPRE	Zhang et al., 2020, Janelia Viral Vector Core	Addgene plasmid # 162378

(*Continued on next page*)

Continued

REAGENT or RESOURCE	SOURCE	IDENTIFIER
Chemicals, peptides, and recombinant proteins		
Clozapine N-oxide	Cayman Chemical	Cat#16882
Clozapine	Cayman Chemical	Cat#12059
HPBCD [(2-Hydroxypropyl)-b-cyclodextrin]	Alfa Aesar	Cat#H31133
Cholera Toxin Subunit B-488	Invitrogen	Cat#C22841
CNQX	Tocris	Cat#0190
RNAscope Probe: *Oprm1*	Advanced Cell Diagnostics	Cat#315841
RNAscope Probe: *Calca*	Advanced Cell Diagnostics	Cat#578771
RNAscope Probe: *Tac1*	Advanced Cell Diagnostics	Cat#410351
RNAscope Probe: *Htr2a*	Advanced Cell Diagnostics	Cat#401291
RNAscope Probe: *Pdyn*	Advanced Cell Diagnostics	Cat#318771
RNAscope Probe: *FoxP2*	Advanced Cell Diagnostics	Cat#428791
RNAscope Probe: *Tacr1*	Advanced Cell Diagnostics	Cat#428781
Deposited data		
Custom MATLAB scripts for data analysis	This paper	Zenodo: https://doi.org/10.5281/zenodo.5685145
Experimental models: Organisms/strains		
Mouse: *Oprm1*-Cre:GFP	Laboratory of Dr. Richard Palmiter	N/A
Mouse: wild type C57BL/6J	Jackson Laboratory	Stock No. 000664
Software and algorithms		
MATLAB	MathWorks	R2019a
Python	Anaconda Distribution	Version 3.7
Doric Neuroscience Studio	Doric Lenses	N/A
RStudio	RStudio	Version 1.2.5001
rEDM	https://cran.r-project.org/web/packages/rEDM/	Version 0.7.2
rEDM	https://ha0ye.github.io/rEDM/	Version 0.7.4
LabChart	ADInstruments	Version 8
EthoVision XT	Noldus Information Technology	Version 12
BZ-X viewer	Keyence	N/A
OlyVIA	Olympus Life Science	N/A
pClamp	Molecular Devices	Version 10
PRISM	GraphPad Software	Version 6
Illustrator	Adobe	Version CS6 and CC2018
Inscopix Data Processing Software	Inscopix	Version 1.6.0.3225
Other		
200um 0.22 NA Fiber-optic Cannula	Laboratory of Dr. Sung Han	N/A
400um 0.37 NA Fiber-optic Cannula	Laboratory of Dr. Sung Han	N/A
ProView™ Integrated Lens 0.6mm x 7.3mm	Inscopix	Cat# 1050-004413

RESOURCE AVAILABILITY

Lead contact

Further information and requests for resources and reagents should be directed to and will be fulfilled by the lead contact, Sung Han (sunghan@salk.edu).

Materials availability

This study did not generate new unique reagents.

Data and code availability

- All data reported in this paper will be shared by the lead contact upon request.
- Original code for fiber photometry and Miniscope single-cell calcium imaging analyses has been deposited at Zenodo and is publicly available as of the date of publication. DOIs are listed in the key resources table.
- Any additional information required to reanalyze the data reported in this paper is available from the lead contact upon request.

EXPERIMENTAL MODEL AND SUBJECT DETAILS

Mouse lines

All protocols for animal experiments were approved by the IACUC of the Salk Institute for Biological Studies according to NIH guidelines for animal experimentation. The *Oprm1-Cre:GFP* transgenic mouse line used in this study was generated by the lab of Dr. Richard Palmiter (Palmiter, 2018), and heterozygous animals were used unless otherwise noted. The wild type mice were purchased from the Jackson Laboratory (Stock No. 000664). Both male and female mice were used in all studies. Animals were randomized to experimental groups, and no sex differences were noted. Mice were maintained on a 12 h light/dark cycle and provided with food and water *ad libitum*.

METHOD DETAILS

Respiratory measurements

Inductance plethysmography

Inductance plethysmography was performed by placing a piezoelectric film beneath the chest of an anesthetized animal, which converted chest movements into voltage signals. Isoflurane was selected for anesthesia for its dose adjustment flexibility and instant feedback. Test mice were kept under light anesthesia until a stable breathing rate of 100-130 bpm—much lower than awake animals—was reached. Breathing rhythm was monitored with inductance plethysmography by placing a piezoelectric sensor beneath the chest of the test mouse to detect the chest expansion that accompanied each breathing cycle. The PowerLab system with LabChart 8 software (ADInstruments) was used for data acquisition, inspiratory and expiratory peak detection, and rate and amplitude calculation. Breathing rate was calculated by counting the number of peaks per minute. Breathing amplitude was estimated by the plethysmograph amplitude, i.e., the height of the plethysmograph waveform. Data were sampled at 100-400 Hz, low-pass filtered at 10 Hz, and smoothed with a 100-ms moving window. Automatic peak detection was validated with manual peak detection.

Whole body plethysmography (WBP)

A custom-built WBP chamber was utilized to measure breathing parameters. The PowerLab system with LabChart 8 software was used for data acquisition, inspiratory and expiratory peak detection, and rate and amplitude calculation. Breathing rate was calculated by counting the number of peaks. Breathing amplitude was estimated by the plethysmograph amplitude, i.e., the height of the plethysmograph waveform. Data were sampled at 1 kHz, band-pass filtered at 1-10 Hz, and smoothed with a 100-ms moving window. Automatic peak detection was validated with manual peak detection.

Mice were placed into the WBP chamber for three 20-min habituation sessions before testing. To test whether thermistor sensor implant alters normal breathing patterns, implanted and naive mice were kept in the WBP chamber for 10-12 min. For chemogenetics experiments, mice were kept in the chamber for 10-12 min during the testing session before and after drug injection. After 5-10 min of chamber habituation, a stable pattern was reached and the averaged value of a stabilized 1-min segment was analyzed.

Micro thermistor-based plethysmography

A custom-built micro thermistor was implanted into the mouse nasal cavity to detect changes in temperature between inspiratory and expiratory airflow (McAfee et al., 2016). In contrast to traditional breathing measurements like whole-body plethysmography (WBP) (Mortola and Frappell, 1998) and tracheostomy airflow sensor measurements, this approach allows us to monitor breathing in awake, unrestrained, behaving mice with unprecedented freedom to access the brain. The sensor was assembled using a Negative Temperature Coefficient (NTC) thermistor (TE Connectivity), an interconnector (Mill-Max), and a voltage divider (Phidgets). PowerLab (ADInstruments) was used for data acquisition, inspiratory and expiratory peak detection, and rate and amplitude calculation. Voltage increases and decreases indicated expiration and inspiration, respectively. Breathing rate was calculated by counting the number of peaks per minute. Breathing amplitude was estimated by the plethysmograph amplitude, i.e., the height of the plethysmograph waveform. Data were sampled at 1 kHz, filtered with a 0.4-25 Hz band-pass filter, and smoothed with a 50-ms moving window. Automatic peak detection was validated with manual peak detection. For the alignment of calcium activity with the onset of major respiratory events, we defined the ‘‘high respiratory activity bout’’ as a continuous period of high activity distinct from the stable baseline that lasts over 120 s.

Stereotaxic surgery

Mice were anesthetized with isoflurane (5% induction, 1.5%–2% maintenance with a nose cone; Dräger Vapor 2000, Draegar) and maintained on a water recirculating heating pad throughout the surgery. Mice were placed on a stereotaxic frame (David Kopf Instruments), the skull was exposed, and the cranium was drilled with a micro motor handpiece drill (Foredom); one or two holes were drilled for viral injection, two holes for screws with implantation, one or two holes for optic fibers, and one hole for a micro thermistor. The virus was injected unilaterally or bilaterally into the PBL [anteroposterior (AP), −1 to −1.15 mm from lambda; mediolateral (ML), ± 1.5 mm; dorsoventral (DV), −3.5 mm, re-zero at the midline with the same AP], unilaterally to the preBötC (AP, −2.4 to −2.6 mm from lambda; ML, 1.3 mm; DV, −5.7 mm from contralateral skull surface), unilaterally or bilaterally to the CeA (AP, −1.1 mm; ML, ± 2.9 mm; DV, −5.2 mm, re-zero at the midline with the same AP), and unilaterally to the dorsal striatum (AP, +0.5 mm; ML, −1.8 mm; DV, −2.2 mm from brain surface). Viral injection was performed with glass pipettes with tips broken for an inner diameter of 20 μm, which were connected to the Nanoject III Programmable Nanoliter Injector (Drummond Scientific) set to an infusion rate of 60 nL/min. Glass pipettes were retracted from the brain 5–10 min after injection. Optic fibers were implanted above the injection site with the DV noted above. The micro thermistor head was carefully lowered into the hole above the nasal cavity (AP, +3.5 mm from the nasal fissure; ML, 0.3 mm). Implants were covered with superglue and dental cement for stabilization. Unless otherwise noted, behavioral experiments were performed three weeks after viral injection and one week after the micro thermistor implantation, and all viruses were obtained from the Salk Institute Viral Vector core.

For fiber photometry, *Oprm1*$^{Cre/+}$ mice were unilaterally injected with 200 nL of either AAV1-syn-FLEX-jGCaMP7s-WPRE (1.5E+13 GC/mL) or control AAV2-EF1a-DIO-eYFP (2.12E+12 GC/mL) virus into the PBL. For the movement-breathing dissociation experiment, we injected 200 nL of AAV1-Syn-GCaMP6f-WPRE-SV40 (2.30E+12 GC/mL) into the dorsal striatum. For investigation of the involvement of PBL *Oprm1*-negative neurons in breathing, we injected 200 nL of AAV8-hSyn-DO-GCaMP6m (UNC viral vector core) into the PBL of the *Oprm1*$^{Cre/+}$ mice. A custom-made stainless-steel mono fiber-optic cannula (400 mm diameter, 0.37 NA) was implanted 0.05 mm above the injection site.

For single-cell calcium imaging with microendoscope, *Oprm1*$^{Cre/+}$ mice were unilaterally injected with 500 nL of AAVDJ-syn-FLEX-jGCaMP8m-WPRE (5E+12 GC/mL) virus into the PBL. An integrated microendoscope lens (0.6 mm x 7.3 mm, Inscopix) was implanted using the following coordinates: AP, −4.95 mm; ML, 1.5 mm; DV, −3.6 mm, re-zero at Bregma.

For chemogenetics, 200 nL of either AAVDJ-EF1a-DIO-hM3D(Gq)-mCherry (6.56E+11 GC/mL), AAVDJ-EF1a-DIO-hM4D(Gi)-mCherry (6.04E+11 GC/mL), or control AAV2-EF1a-DIO-eYFP (2.12E+12 GC/mL) was injected bilaterally into the PBL of *Oprm1*$^{Cre/+}$ mice.

For optogenetics, mice were bilaterally injected with 200 nL of AAVDJ-EF1a-DIO-hChR2(H134R)-EYFP-WPRE-pA (1.8E+13 GC/mL) for photostimulation, 300 nL of AAVDJ-FLEX-ArchT-GFP (1.26E+12 GC/mL) for photoinhibition, or a corresponding amount of control AAV2-EF1a-DIO-eYFP (2.12E+12 GC/mL) into the PBL of *Oprm1*$^{Cre/+}$ mice. A custom-made ceramic mono fiber-optic cannula (200 mm diameter, 0.22 NA) was implanted 0.3 mm above the injection site.

For monosynaptic rabies tracing of PBL^{Oprm1} neurons, 200 nL of AAV8-hSyn-FLEX-TVA-P2A-GFP-2A-oG (3.64E+13 GC/mL) was injected unilaterally into the PBL of the *Oprm*$^{Cre/+}$ mice or control wild type mice. After three weeks, 200 nL of EnvA-DG-rabies-mCherry (3.95E+08 GC/mL) was unilaterally injected into the PBL. Mice were sacrificed seven days following injection.

For investigation of PBL^{Oprm1} projections to the ventrolateral medulla, *Oprm*$^{Cre/+}$ mice were bilaterally injected with 200 nL of AAV2-phSyn1(S)-FLEX-tdTomato-T2A-SypEGFP-WPRE (2.23E+11 GC/mL) into the PBL. Euthanasia and histology were performed three weeks following injection.

For intersectional anatomical tracing and projection-specific electrophysiology, *Oprm*$^{Cre/+}$ mice were bilaterally injected with 200 nL of AAVrg-EF1a-DIO-FLPo-WPRE-hGHpA (1.98E+13 GC/mL) unilaterally into the preBötC, 200 nL of AAVrg-EF1a-DIO-mCherry (1.51E+13 GC/mL) unilaterally into the CeA, and 200 nL of AAV9-EF1a-fDIO-hChR2(H134R)-EYFP (5.21E+12 GC/mL) unilaterally into the PBL.

For projection-specific fiber photometry calcium activity recording, *Oprm*$^{Cre/+}$ mice were bilaterally injected with 200 nL of AAVrg-EF1a-DIO-FLPo-WPRE-hGHpA (1.98E+13 GC/mL) unilaterally into the preBötC or into the CeA, and 200 nL of AAV8-Ef1a-fDIO-GCaMP6s (1.0E+13 GC/mL) unilaterally into the PBL. A custom-made zirconia mono fiber-optic cannula (400 mm diameter, 0.37 NA) was implanted 0.05 mm above the injection site and a breathing sensor was implanted into the nasal cavity.

For projection-specific optogenetics, *Oprm*$^{Cre/+}$ mice were injected with 200 nL of AAVrg-EF1a-DIO-FLPo-WPRE-hGHpA (1.98E+13 GC/mL) unilaterally into the preBötC or bilaterally into the CeA, and 200 nL of AAV9-EF1a-fDIO-hChR2(H134R)-EYFP (5.21E+12 GC/mL) or control AAV8-EF1a-fDIO-EYFP (4.39E+12 GC/mL) bilaterally into the PBL. Unilateral injection was made into the preBötC to minimize damage to the medulla. A custom-made ceramic mono fiber-optic cannula (200 mm diameter, 0.22 NA) was implanted 0.5 mm above the injection site.

For projection-specific chemogenetics, *Oprm*$^{Cre/+}$ mice were injected with 200 nL of AAVrg-EF1a-DIO-FLPo-WPRE-hGHpA (1.98E+13 GC/mL) unilaterally into the preBötC or bilaterally into the CeA, and 250 nL of AAVDJ-hSyn-fDIO-hM4D(Gi)-mCherry-WPREpA (1E+13 GC/mL) or control AAV8-EF1a-fDIO-EYFP (4.39E+12 GC/mL) bilaterally into the PBL.

Fiber photometry

A fiber photometry system (405 and 465 nm Fiber Photometry System, Doric for Figures 1 and S1G; pyPhotometry for other figures) was used to record PBL^{Oprm1} activity. For the Doric system, GCaMP isosbestic fluorescence (405 nm excitation) and calcium-dependent fluorescence (465-nm excitation) were recorded at a sampling rate of 12 kHz, and data were analyzed with the Doric Neuroscience Studio software. For the pyPhotometry system, both channels were recorded with the 1-color time-division setting at 100 Hz with its provided Python script, and data were analyzed with custom MATLAB scripts. Baseline fluorescence was calculated by a least mean squares fitting of the 405-nm channel in reference to the 465-nm channel, and the relative change in fluorescence ($\Delta F/F$) was calculated as: $(F_{465}\text{-}F_{405\_fitted})/F_{405\_fitted}$.

Cross-correlation analysis between calcium signals and respiration data was performed using the z-scored data and the MATLAB "xcorr" function with the normalized option, which allows autocorrelations at zero lag to equal 1. The area under the curve (AUC) was calculated with the MATLAB "trapz" function with the z-scored data.

In awake behaving animals, concurrent measurements of PBL^{Oprm1} activity and respiration were recorded in the animal's home cage for 20 min. For sighing analysis, sighing events were identified based on the stereotypical voltage pattern from the breathing recording. For sniffing analysis, rearing-sniffing events were identified based on the video recording. For pinching test, fine forceps were used to deliver a transient tail pinch to the test animal in its home cage 5-6 times with at least 1-min inter-trial interval. Behavioral video recording and synchronization were performed with Raspberry Pi camera (Raspberry Pi Foundation). For hot plate test, animals were placed on a 55°C hot plate custom-built with a TC-720 thermoelectric temperature controller (TE Technology) for four min.

In anesthetized animals, we recorded PBL^{Oprm1} activity and respiration simultaneously during the delivery of mechanical and thermal pain. For mechanical stimuli, 0 g and 300 g of mechanical pressure were delivered to the tail tip using a dial tension gauge (ATG-300-1, Vetus Instruments). For thermal stimuli, 25°C and 55°C heat were administered to the tail tip using a rod connected to a temperature controller (TA4-SNR+K, Mypin). Painful stimuli were delivered for 5 s after a stable 10 s baseline. AUC was calculated for 0–2.5 s before, 2.5–5 s after the mechanical or thermal stimulation, and during the 2-min segment before and after the start of temperature change during the hot plate assay.

Single-cell calcium imaging

Calcium activities were recorded at 10 Hz and 0.4–1 mW/mm^2 LED power using an Inscopix nVista miniature microscope. Animals were attached to both the breathing sensor and the miniscope, and allowed to habituate in the home cage three times before the actual recording. During the recording, animals freely explored the home cage for 20 min while their breathing pattern, calcium activity, and behavior were being recorded. On subsequent imaging sessions, the breathing sensor was removed to reduce the weight of the head attachments, and fine forceps were used to briefly pinch animals' tails 5-6 times. A Raspberry Pi camera was used to record behavior videos and trigger calcium and breathing recordings. Pinching onsets were manually identified from the behavioral video. Inscopix data processing software was used for data post-processing with 2x spatial downsampling, fixing the defective pixels, spatial band-pass filtering, and motion correction using the first frame as the global reference frame. Single cells were identified by the CNMFe algorithm and then validated manually. The output unit was dF over noise and z-scored throughout the whole trace.

For heatmap, we plotted representative breathing trace and averaged pinching trace for each individual cell from one example animal. Cells were sorted by the average value in the breathing trials, and the pinching trials were plotted in the same order. To classify cells that responded to breathing, we generated a series of pairwise CCM models in which the inputs were each neuron's activity and the animal's breathing rate, and the outputs were the predictability scores of each pair. The neurons whose activities displayed a predictive relationship with breathing were classified as "breathing-responsive cells." To identify cells that responded to pinching, we calculated the maximum or minimum values during 0-4 s before and 0-10 s after pinching for each episode and compared "pre" and "post" groups with paired t tests. Neurons that showed significant differences in the statistical tests were classified as pain responsive.

Convergent cross-mapping

State-space reconstruction models were generated using the convergent cross mapping framework (Sugihara et al., 2012), a nonlinear time series embedding method (Sugihara and May, 1990) based on the Takens theorem and its generalized form (Deyle and Sugihara, 2011), which builds low-dimensional manifolds from time series and makes predictions across variables. Analysis and predictions were calculated using the R package rEDM 0.7.2 (https://cran.r-project.org/web/packages/rEDM/) for evaluation and the rEDM 0.7.4 (https://ha0ye.github.io/rEDM/) for model predictions in the RStudio environment. These packages were run on a dual Intel Xeon Gold 6148 Server with 384GB RAM or an Intel Core i9 2.4 GHz MacBook Pro with 32 GB RAM. Key parameters were determined individually by lagged coordinate embedding using the simplex function implementation in rEDM to optimize predictive skill as measured by the predicted over observed rho. Parameters include the delay tau, which calculates the characteristic timescale of the series, and the embedding dimensionality, which estimates the number of variables driving the system and approximates variable number as given by the Whitney embedding theorem (Whitney, 1936) as minimally equal to the real number n of variables, but no more than two times n + 1 ($n \leq E \leq 2n+1$). The choice of tau was informed by minimizing mutual information (Fraser and Swinney, 1986). This approximately corresponds to an autocorrelation of ~0.3, which was applied if data maximized predictive skill across datasets. To prevent data contamination, an exclusion radius was applied that was larger than the respiration rate smoothing window of five timesteps. When data allowed, an exclusion radius of E*tau was applied. If not, the exclusion radius was set just larger than tau. In this paper, CCM was utilized to generate multidimensional models from embeddings of GCaMP activity which were used to predict breathing rate, or vice versa.

Chemogenetics

For behavioral testing, CNO (Cayman Chemical) was diluted in 0.9% saline to make a 1 mg/mL working solution. No precipitate was observed in the solution, indicating that the specific polymorph of the drug exhibits sufficient water solubility. CNO solution was injected intraperitoneally with a final concentration of 5 mg/kg (for whole population breathing measurement and all projection-specific silencing experiments) or 7.5 mg/kg (for whole population silencing experiments). Behavioral testing began 45-60 min after CNO injection. Animals that did not exhibit expression on one side were excluded.

For medullary activation of PBL^{Oprm1} projections, clozapine, a high-affinity agonist for DREADDs (Gomez et al., 2017), was used to activate the PBL^{Oprm1} axon terminals in the ventrolateral medulla (VLM) breathing center. eYFP-expressing controls ensured that CLZ selectively activated DREADD-expressing neurons. CLZ was first solubilized at pH 2.0 with HCl and then diluted. HPBCD [(2-Hydroxypropyl)-b-cyclodextrin] was added to solubilize clozapine with an HBPCD:CLZ molar ratio of 4:1. Solutions were titrated to neutral pH using NaOH and filter sterilized (0.22 mm) prior to intracranial administration (Abrams et al., 2008). CLZ (1 μg/μL) was injected bilaterally to the VLM with 100 nL/side using a glass pipette. A 50-nL aliquot of Cholera Toxin Subunit B-488 was injected using the same coordinates to mark the injection site. Data from 0–3 min before and 7–10 min after CLZ injection were used for quantification.

Ex vivo electrophysiology

Mice were anesthetized with isoflurane and the vascular system was perfused with ice-cold cutting solution (110.0 mM choline chloride, 25.0 mM $NaHCO_3$, 1.25 mM NaH_2PO_4, 2.5 mM KCl, 0.5 mM $CaCl_2$, 7.0 mM $MgCl_2$, 25.0 mM glucose, 5.0 mM ascorbic acid and 3.0 mM pyruvic acid, bubbled with 95% O_2 and 5% CO_2). Mice were decapitated, and brains were quickly removed and chilled in ice-cold cutting solution. Coronal slices containing the PBL (250 mm) were cut using a VT 1200S Vibratome (Leica) and transferred to a storage chamber containing artificial cerebrospinal fluid (aCSF; 124 mM NaCl, 2.5 mM KCl, 26.2 mM $NaHCO_3$, 1.2 mM NaH_2PO_4, 13 mM glucose, 2 mM $MgSO_4$ and 2 mM $CaCl_2$, at 32°C, pH 7.4, bubbled with 95% O_2 and 5% CO_2). After recovery of at least 30 min, slices were transferred to room temperature (22 - 24°C) for at least 60 min before use.

Slices were transferred into the recording chamber and perfused with aCSF at a flow rate of 2 mL/min. The temperature of the aCSF was controlled at 32°C by a TC-324C Temperature controller (Warner Instruments). PBL^{Oprm1} neurons were visualized with 490 nm epifluorescence illumination with a Scientifica SliceScope Pro (Scientifica). Whole-cell and cell-attached patch-clamp electrophysiology was performed with Multiclamp 700B amplifiers (Molecular Devices). Signals were digitized at 10 kHz with Digidata 1550B (Molecular Devices).

For cell-attached patch-clamp, aCSF was the internal solution. Spontaneous firing was measured before and after a 3 mM CNO perfusion. For whole-cell patch-clamp recordings, K^+-containing internal solution was used (130 mM K-gluconate, 20 mM HEPES, 2 mM NaCl, 4 mM $MgCl_2$, 0.25 mM EGTA, 4 mM Na-ATP, 0.4 mM Na-GTP, pH 7.2). Under current-clamp conditions, a 50 pA current was injected into the cell to induce action potential firing before and after a 3 mM CNO perfusion.

For the projection-specific electrophysiology experiment, 2 ms blue light pulse was emitted from a collimated 473 nm light-emitting diode (pE-300, CoolLED) under the control of an Axon Digidata 1440A Data Acquisition System and pClamp 10 software (Molecular Devices). Light was delivered through the reflected light fluorescence illuminator port and a 40X objective. AMPA-mediated EPSCs were blocked by bath application of 10 mM CNQX (Tocris). Quantitation was performed with the Clampfit module in the pClamp 10 software.

Optogenetics

For photostimulation and photoinhibition, a 470 nm collimated diode and a 589 nm diode-pumped solid-state (DPSS) laser system (LaserGlow Tech.) were used. For breathing measurements, mice were placed under light isoflurane anesthesia and subjected to either 470 nm photostimulation at 20 Hz or continuous 589 nm photostimulation to activate or silence PBL^{Oprm1} neurons. The selection of pulsed and continuous light was determined to optimize the excitation and inhibition experiments, respectively. In general, light-driven ion pumps, such as halorhodopsin and archaerhodopsin both require continuous light to sustain the ion pumping activity (Mahn et al., 2021; Zhang et al., 2007). Particularly, ArchT has a fast photocycle and quickly recovers from the opening state in the dark (Chow et al., 2012; Chow et al., 2010). Pulsed light was used for ChR2-mediated excitation since this is sufficient for activating the neurons of interest while reducing tissue heating (Stujenske et al., 2015). The output power was 5 ± 1 mW, as measured from the tip of the optic fiber. For investigation of ChR2-induced breathing changes, 5-ms square pulses were given at 20 Hz for 10 s. The maximum breathing parameters 10 s before and 10 s after the stimulation onset were analyzed. For ArchT-induced breathing changes, a 30 s continuous-wave stimulation was delivered, and the average breathing parameters 10 s before and 10 s after the stimulation onset were analyzed.

For behavioral tests with projection-specific optogenetic activation experiments, the output power was 10 ± 2 mW, as measured from the tip of the optic fiber, and 2-ms square pulses at 40 Hz were given with different burst patterns (RTPA: 2 s on, 10 s off; formalin: 1 s on; 3 s off; EPM: 2 s on, 2 s off; other assays: continuous).

For ArchT-stimulation combined with mechanical and thermal pain stimulation, 300 g of mechanical pressure and 55°C heat were administered to the mouse tail tip using a dial tension gauge (ATG-300-1, Vetus Instruments) and a temperature controller (TA4-SNR+K, Mypin), respectively. Painful stimuli were administered for 5 s after a stable 10 s baseline, and a subsequent 5 s photoinhibition was administered for 3–5 s. For quantification purposes, three 3 s breathing episodes were analyzed: immediately before and immediately after the painful stimuli, and during the 5 s photostimulation.

For the ArchT- and ChR2- stimulation combined with the RTPP or RTPA assay, a two-chamber arena (30 × 60 × 30 cm^3) was used. A Gigabit Ethernet (GigE) USB camera (DFK 33GX236, Imagine Source; 25 frames/s, FPS), together with video-tracking software (EthoVision XT 12, Noldus Information Technology), tracked the animal and controlled the stimulation. After connecting to the patch cord, mice were placed in one side of the chamber for a 10 min baseline session and a subsequent 10 min test session, where a continuous wave of photoinhibition (ArchT) or 40 Hz photostimulation (ChR2) was administered when mice entered one side of the chamber. The stimulation side was counterbalanced among animals. A 70% ethanol solution and deionized water were used for cleaning immediately after each test. For the ArchT experiment, animals that did not show bilateral expression were excluded from the analysis.

Histology

Mice were euthanized with CO_2 at a flow rate of 1.2 L/min (LPM), perfused intracardially with ice-cold phosphate-buffered saline (PBS), and fixed with 4% paraformaldehyde (PFA, 19210, Electron Microscopy Sciences) in phosphate buffer (PB). The brain was extracted, post-fixed in 4% PFA overnight, and dehydrated in 30% sucrose in PBS until sliced. Frozen brains were cut into 50-μm coronal slices using a CM 1950 cryostat (Leica) and stored in PBS prior to mounting. The slices were mounted on Superfrost microscope slides (Fisher Scientific) with DAPI Fluoromount-G mounting media (Southern Biotech) for imaging.

Immunohistochemistry

To investigate PBL^{Oprm1} projections onto preBötC neurons, anti-somatostatin (SST, a marker for preBötC) and anti-choline acetyltransferase (ChAT, a marker for motor neurons in the nearby nucleus ambiguous) staining was performed on medulla (AP −7.3 mm, coronal) sections. To confirm MOR expression on the jGCaMP7s-expressing cells or Rabies tracing starter cells, anti-MOR staining was performed on parabrachial sections. Mice were euthanized with CO_2 at a flow rate of 1.2 LPM, then perfused intracardially with ice-cold PBS and followed by 4% PFA in PB. The brain was extracted, post-fixed in 4% PFA overnight, and dehydrated in 30% sucrose in PBS until sliced. Frozen brains were cut into 30 μm coronal slices with a CM 1950 cryostat and stored in PBS. For anti-MOR staining, slices were treated in 1% SDS at room temperature for 5 min for antigen retrieval.

Sections were washed with 0.2% PBST and blocked with 3% NDS (or 5% NDS in 0.3% PBST for anti-MOR) for 1 h at room temperature. After rinsing with PBST, slices were incubated with rabbit anti-SST14 (1:250, Peninsula Laboratories) and goat anti-ChAT (1:100, Sigma-Aldrich), or rabbit anti-MOR (1:250, Immunostar) at 4°C for 24 h. The following day, brain tissues were rinsed with PBST and incubated in Cy3-conjugated Donkey Anti-Rabbit IgG and Alexa Fluor 647-conjugated Donkey Anti-Goat IgG (1:500 in 3% NDS, for SST/ChAT staining) or Alexa Fluor 647-conjugated Donkey Anti-Rabbit IgG (1:300 in 5% NDS, for MOR staining) for 90 min at room temperature. After washing with PBS, the slices were mounted on Superfrost microscope slides with DAPI Fluoromount-G mounting media for imaging.

RNA *in situ* hybridization

RNA *in situ* hybridization was performed using the RNAscope Fluorescent Multiplex Assay using the probes and kits purchased from Advanced Cell Diagnostics. Brains were collected from wild type mice and immediately frozen with 2-methylbutane chilled with dry ice. Frozen brains were cut into 20-μm coronal slices with a CM 1950 cryostat and directly mounted onto the Superfrost Plus Microscope Slides (Fisher Scientific). Sample preparation, pretreatment, and signal detection were performed according to the ACD protocols.

For quantification, one representative image from the PBL were selected from n = 5-6 mice, and all fluorescent cells within a field of view of 600 μm x 600 μm were included. DAPI-stained nuclei were first identified, then the cell contour was defined with a ~2-μm radius surrounding the DAPI signals. Cells containing at least five puncta inside the imaginary boundary were labeled as positive.

Imaging

Images for histological confirmation were taken with the BZ-X710 all-in-one fluorescence microscope with the BZ-X viewer software under a 10X, 0.45 NA objective (Keyence). Images for the monosynaptic Rabies tracing were taken at the Salk Institute Waitt Advanced Biophotonics Core with the Olympus VS-120 Virtual Slide Scanning Microscope under an Olympus UPLSAPO 4X, 0.16 NA objective. Images for MOR immunohistochemistry, SypGFP terminals in the preBötC, projection mapping, and RNAscope were taken by an FV3000 Confocal Laser Scanning Microscope with FV31S-SW software under Olympus UPLSAPO 4X, 0.16 NA; 10X, 0.40 NA; 20X, 0.75 NA; 40X, 1.30 NA, or 60X, 1.42 NA objectives (Olympus). For quantification, images were processed with the same gain, offset, and exposure time.

Monosynaptic rabies tracing

Brain slice collection and region assignments were performed according to the Allen Brain Atlas. Every 50 mm section from AP + 2.62 mm to AP −7.455 mm was collected and imaged by an Olympus VS-120 Virtual Slide Scanning Microscope using the OlyVIA software with identical magnification and exposure time. Neurons with mCherry-positive cell bodies were counted manually. Brain slices located ± 0.4 mm anterior and posterior to the starter region were excluded. The injection was unilateral (right side), and the quantification of cells was bilateral. The percentage of the total presynaptic inputs from a given brain region was calculated by dividing the number of presynaptic neurons by all neurons registered to the atlas. For quantification of starter cells with MOR immunohistochemistry, a field of view of 300 mm x 300 mm from the PBL area was used for counting.

Subpopulation-specific anatomical mapping

To reveal the expression patterns of PBL^{Oprm1} subpopulations, brain slices containing the PBL (50-mm thickness) were collected three weeks after viral injection. In the PBL, mCherry- and eYFP-labeled cells as well as their overlaps were counted, and the average cell numbers of three slices were displayed. To investigate projection patterns of PBL^{Oprm1} subpopulations, brain sections (30-mm thickness for sections containing ventrolateral medulla, 50-mm thickness otherwise) were collected three weeks after viral injection. SST immunohistochemistry was performed in medullary slices to identify the preBötC area.

Elevated plus maze test

To measure anxiety-like behavior, a custom-built plus-shaped maze with two 77 cm long opposite closed arms, two 77 cm long opposite open arms, and a central square of 7 cm sides was situated 70 cm above the floor. EthoVision XT 12 software with a GigE USB camera at 25 FPS was used for animal tracking. The test mouse was introduced to the open arm adjacent to the center and explored the maze for 5 min. For the ChR2 experiment, mice were connected with patch cord, put back into the home cage for 10 min, then introduced to the arena. Time spent in open and closed arms and entries into open arms were calculated by the EthoVision XT 12 software. A 70% ethanol solution and deionized water were used for cleaning immediately after each test. For hM4Di experiments, to reduce open arm time for control animals, we used bright lighting and opaque walls of closed arm. For ChR2 experiments, to increase open arm time for control animals, we used dim lighting and transparent walls of closed arm.

Hot plate test

To measure thermal sensitivity, mice were placed inside a cylindrical, transparent Plexiglass chamber (D = 11 cm, H = 15 cm) on a hot plate (52°C or 55°C, PE34, IITC Life Science). For hM4Di experiments, the temperature was set to 55°C; the latency of the painful response (hind paw shake, lick or jump) was manually recorded until the animal jumped out or until the animal stayed on the hot plate for 60 s; for ChR2 experiments, the temperature was set to 52°C, and a lid was put on top of the cylinder to prevent the animal from jumping out. The number of jumps was manually recorded for 50 s.

Electronic von Frey test

To measure mechanical sensitivity, the Dynamic Plantar Aesthesiometer (37450, Ugo Basile, Italy) was used and was set to maximum force of 50 g after 20 s. Mice were habituated inside a Plexiglass chamber (10 × 10 × 13 cm) on a metal mesh floor for > 2 h until they were awake but largely immobile. The metal rod was placed underneath the left hind paw. The system automatically measured the latency and force delivered upon paw withdrawal. This measurement was taken five times with > 1 min intervals. The averaged value was analyzed.

Formalin test

To measure affective pain response, 10 μL of 4% formalin (for hM4Di assays) or 1% formalin (for ChR2 assays) was injected subcutaneously in the left hind paw of an awake mouse. Mice were placed in a Plexiglass chamber (10 × 10 × 13 cm) with a mirror placed behind it. Formalin injection produced a biphasic pain response over a 1 h test period consisting of licks, twitches, and raising or shaking of the injected paw. The number of licks and time spent licking during each 5-min bin were scored through the 1 h section. The responses during the acute (0–5 min following injection) and the inflammatory phase (20–35 min following injection) were further calculated.

Contextual fear conditioning

The fear conditioning chamber (ENV-007CT, MED Associates) is an arena (26 × 30 × 33 cm) with two Plexiglass walls, two metal walls, and a metal grid floor to deliver electrical shocks (ENV-005, MED Associates). The chamber was connected to a standalone aversive stimulator (ENV-414S, MED Associates) and enclosed in a light- and sound- attenuating cubicle (ENV-018MD, MED Associates). EthoVision XT 12 software with a GigE USB camera with 25 FPS tracked the animal. A 70% ethanol solution and deionized water were used for cleaning immediately after each test. On days 1 and 2, mice underwent two 6-min habituation sessions in the chamber. On day 3, mice were introduced to the chamber 45–60 min after CNO injection and subsequently received five shocks (2 s, 0.2 mA) with uneven intervals over a 7 min trial. After 24 h, mice were reintroduced to the chamber for a 2-min context-dependent retrieval test. The percentage of time frozen and the total distance moved during each session were calculated by the EthoVision XT 12 software. Freezing behavior was defined as the period during which the velocity of the mouse was less than 1.75 cm/s for at least 3 s. Automatic scoring was validated with manual scoring.

Open field test

A 40 × 40 cm open field arena was used to measure anxiety-like behaviors and general locomotion. Animals were introduced into the center of the open field arena and left to explore the arena for 5 min. Total distance moved, time spent in the center (20 × 20 cm), and entries into the center were measured.

Freezing measurement

For freezing measurement in the projection-specific optogenetics experiment, a 20 × 20 cm chamber was placed in the center of the open field arena. 470 nm laser was triggered with a pattern of 1-min off, 30 s on four times. Freezing behavior was defined as the period during which the velocity of the mouse was less than 1.75 cm/s for at least 3 s. Automatic scoring was validated with manual scoring.

Breathing measurement with pain or anxiety tests

To measure breathing changes under different levels of foot shock stimuli, mice were placed inside a cylindrical, transparent Plexiglass chamber (D = 11 cm, H = 15 cm) inside the fear conditioning chamber (26 × 30 × 33 cm). For the low baseline breathing condition, animals were allowed to habituate for 20-40 min until the baseline breathing rate became lower than 300 bpm. 0.2 mA or 0.04 mA foot shocks were given for 2 s. To measure breathing changes during the elevated plus maze assay, mice implanted with thermistor sensors were attached to the patch cord and put back into their home cages for a 10-min habituation. Then the test mouse was introduced to the elevated plus maze with transparent walls under a low lighting condition. To measure breathing changes during the elevated platform assay, mice implanted with thermistor sensors were attached to the patch cord, put back into their home cage for baseline recording, and then placed onto an elevated platform (10-cm diameter transparent dish) 100 cm above the floor. Breathing was measured with the thermistor sensor, and velocity and location were measured by the EthoVision XT 12 software. To measure breathing changes during the formalin assay, mice implanted with thermistor sensors were attached to the patch cord and put into the Plexiglass chamber (10 × 10 × 13 cm). After 30 min habituation, 5 mg/kg CNO was injected i.p. into the test mouse. After 30 min, 10 μL of 4% formalin was injected subcutaneously into the hind paw. The averaged breathing rate during the acute phase (0 –5 min following formalin injection), and the inflammatory phase (15– 25 min following injection) were further calculated. The delta breathing rate was calculated by subtracting the averaged rate during the 5 min before each phase.

QUANTIFICATION AND STATISTICAL ANALYSIS

Quantifications of breathing measurement, fiber photometry, optogenetics, chemogenetics, behavioral tests, and monosynaptic rabies tracing are described in the corresponding sections of text and methods. All data are presented as mean ± SEM. Data were analyzed using either a Student's t test, one-way ANOVA with Tukey's post hoc comparison, or two-way ANOVA with Bonferroni's post hoc comparison. All statistical analyses were performed with Prism 6 (GraphPad). Statistical significance was defined as follows: ns, not significant; *, $p < 0.05$; **, $p < 0.01$; ***, $p < 0.001$; ****, $p < 0.0001$. Full details of statistical tests in individual figures are described in the figure legend.